

Statistical Properties of Radio Halos in Galaxy Clusters and Origin of Seed Electrons for Reacceleration

KOSUKE NISHIWAKI¹ AND KATSUAKI ASANO¹

¹*Institute for Cosmic Ray Research, The University of Tokyo, 5-1-5 Kashiwanoha, Kashiwa, Chiba 277-8582, Japan*

(Received; Revised; Accepted)

Submitted to ApJ

ABSTRACT

One of the most promising mechanisms for producing radio halos (RHs) in galaxy clusters is the reacceleration of cosmic-ray electrons by turbulences. However, the origin of the seed electrons for the reacceleration is still poorly constrained. In the secondary scenario, most of the seed electrons are injected via collision of proton cosmic-rays, while high-energy electrons are directly injected in the primary scenario. In this paper, we examine the two scenarios for the seed electrons with the observed statistical properties of RHs, combining two methods: following the temporal evolutions of the electron energy and radial distributions in a cluster, and the merger history of clusters. We find that the RH lifetime largely depends on the seed origin, as it could be longer than the cosmological timescale in the secondary scenario. We study the condition for the onset of RHs with the observed RH fraction and the RH lifetime we obtained, and find that long-lived RHs in the secondary scenario should be originated from major mergers with a mass ratio of $\xi \sim 0.1$, while the short lifetime in the primary scenario requires more frequent onsets by minor mergers with $\xi \sim 0.01$. Our simple model of the turbulence acceleration can reproduce the observed radio luminosity-mass relation. The RH luminosity functions we obtained suggest that the expected RH number count with the ASKAP survey will detect $\approx 10^3$ RHs in both the scenarios.

Keywords: Galaxy clusters (584)

1. INTRODUCTION

An increasing number of galaxy clusters are found with diffuse cluster-scale synchrotron emission in the radio band. Giant Radio halos (RHs) are the Mpc-sized emission often found in the central region of massive clusters (see [van Weeren et al. 2019](#), for a review). The progress in the RH observation has been achieved with the NRAO VLA Sky Survey (NVSS, [Giovannini et al. 1999](#)), the Giant Meterwave Radio Telescope (GMRT, [Venturi et al. 2007](#)) and its extension ([Kale et al. 2013](#)). A novel progress in this field is now ongoing with current generation of high-sensitivity radio telescopes, such as LOw Frequency ARay (LOFAR, [van Haarlem et al. 2013](#)) and the the pathfinders for Square Kilometer Ar-ray (SKA, [Dewdney et al. 2009](#)).

A variety of statistical properties of RHs have been reported. For example, the occurrence of RHs correlates with the dynamical disturbance of clusters observed in X-ray (e.g., [Schuecker et al. 2001](#); [Cassano et al. 2010, 2013](#); [Cuciti et al. 2021a](#)), and the radio luminosity is

known to correlate with the X-ray luminosity or the mass measured with the Sunyaev-Zel'dovich (SZ) effect (e.g., [Cassano et al. 2013](#)). In addition, those correlations show bimodalities, as the clusters without RHs fall well below the relations ([Brunetti et al. 2007](#)). The occurrence of RHs seems to increase with the mass of the cluster ([Cuciti et al. 2015, 2021a](#)). Those facts indicate a firm connection between the formation process of galaxy clusters and the non-thermal components in the intra-cluster medium (ICM).

During the structure formation of galaxy clusters, a part of the gravitational potential energy would be dissipated into the acceleration of relativistic particles by the merger. In the so-called turbulent reacceleration model, RHs originate from the reacceleration of seed cosmic-ray electrons (CREs) by the merger-induced turbulence (e.g., [Brunetti et al. 2001](#); [Petrosian 2001](#); [Fujita et al. 2003](#)). As the turbulence could permeates the most of the cluster volume, this model can explain the large extension of the radio emission. This model is supported by the observational signature of the turbulence accel-

eration such as the steep spectral index ($F_\nu \propto \nu^{-\alpha_{\text{syn}}}$ with $\alpha_{\text{syn}} \approx 1.5$) or the break feature in the radio spectrum (e.g., Brunetti et al. 2008; Macario et al. 2010). However, the origin of the seed electrons for the reacceleration has not been revealed yet (e.g., Brunetti & Jones 2014).

There are two possible origins of the seed CREs. One is the *primary* scenario, where CREs are directly injected by accelerators like large-scale accretion shocks, or escaped from radio jets launched from the central active galactic nuclei (AGNs) (e.g., Kang et al. 2012; Völk & Atoyan 1999; Gitti et al. 2002; Heinz et al. 2006). The other is the *secondary* scenario, where the primary CRE injection is dominated by the secondary injection from the pp collisions between cosmic-ray protons (CRPs) and thermal protons in the ICM (e.g., Denison 1980; Blasi & Colafrancesco 1999; Brunetti & Blasi 2005; Kushnir & Waxman 2009). Recently, by modeling the well-studied RH in the Coma cluster, we have found that the non-thermal properties, such as the CR energy density and the location of the primary CR accelerators, could be significantly different between those two scenarios, which could be a clue to reveal the seed origin (Nishiwaki et al. 2021). In this study, we further discuss possible differences appearing in the statistics of RHs.

The luminosity function of RHs has been calculated with the scaling relation between the radio power and the mass or X-ray luminosity (e.g., Enßlin & Röttgering 2002). Several theoretical attempts have been made to investigate the occurrence of RHs. In the context of the reacceleration scenario, Cassano & Brunetti (2005) constructed a self-consistent statistical model for the turbulent injection and the RH generation during the cluster evolution. Their model is constrained by the observed occurrence of 30% around 1.4 GHz, and predicts a much smaller RH fraction ($\leq 5\%$) in less massive clusters. The increased occurrence at lower frequencies (≈ 100 MHz) is predicted in Cassano et al. (2010). The bimodality in the RH luminosity distribution may be explained with the rapid CR streaming or diffusion rather than the reacceleration. Cassano et al. (2016) pointed out that the lifetime of RHs and the critical mass ratio for the reacceleration onset can be constrained from the observed fraction of radio-loud clusters with the merger rate of the dark matter halo obtained in N-body simulations. Zandanel et al. (2014) proposed the combined scenario, where the emission in the core region is produced by the secondary CREs, while the outer parts are dominated by primary CREs.

The main objective of this paper is to investigate how the statistical properties found in the RH observations

provide constraints on those different scenarios for the seed population. In this paper, we combine following two methods; the time-dependent calculation of the CR spectral evolution solving the Fokker-Planck equation, and the Monte Carlo (MC) procedure to simulate the macroscopic cluster evolution through mergers and the mass accretion. In the former calculation, we consider the reacceleration of CRs and compare the two scenarios, secondary or primary, of the CRE injection (Section 2). Those models are constrained by the observed spectrum and spatial profile of the Coma RH (Section 2.5). With this method, we can estimate how different the lifetime of the radio emission is between the secondary and primary scenarios (Section 3).

In the latter part, we construct the MC merger tree from the halo merger rate based on N-body simulations (Section 4). Considering the lifetime obtained from the former part, we investigate consistent conditions for the onset of RHs with the observed statistics for both the two scenarios (Section 5). Our attempt requires that the peak radio luminosity after a merger is related to the cluster mass scale. The required correlation is partially justified in Section 7, where we again solve the evolution of CRs in RHs with various masses, assuming a scaling between the acceleration efficiency and the cluster mass. Finally, the detectability of low-mass RHs with upcoming radio observations is discussed in Section 9.

Throughout this paper, we assume the Λ CDM cosmology and adopt the parameters from Planck Collaboration et al. (2020), where $H_0 = 67$ km/s/Mpc ($h = 0.67$ or $h_{70} = 0.96$), $\Omega_m h^2 = 0.143$ and $\Omega_\Lambda = 0.68$.

2. TIME EVOLUTION OF COSMIC-RAY DISTRIBUTION

First, we study the emission lifetime of RHs in the turbulent reacceleration model. For this purpose, we integrate the Fokker-Planck (FP) equation for the CR distribution function and follow the time evolution of the synchrotron spectrum. We mainly discuss the comparison of the two scenarios for the origin of seed CREs, i.e., the primary scenario and the secondary scenario. Those scenarios are distinguished by the injection rate of primary cosmic-ray protons (CRPs) relative to that of CREs. Our model here is basically the same as Nishiwaki et al. (2021), which includes both the reacceleration and the spatial diffusion of CRs. We adopt the observed property of the Coma RH, for which we have well-examined data sets, to constrain the model parameters.

Our model is one-dimensional in space, which enable us to follow the evolution of brightness profile in addi-

tion to the spectral evolution. In our previous study, the large extension of the RH was explained with the radial dependence in the CR injection with a constant reacceleration efficiency in space. In this paper, we investigate another possibility: the radial dependence in the reacceleration efficiency for a fixed injection profile. While both the models well reproduce the Coma RH, the spectral evolution or the lifetime is not largely affected by the injection or reacceleration efficiency profile. Our model includes relatively less parameters and it is easy to apply to other RHs with different masses (Section 7).

2.1. The Fokker-Planck equation

We solve the isotropic one-dimensional Fokker-Planck (FP) equation to follow the time evolution of the distribution function in the phase space, $N_s(r, p, t) = (4\pi r^2)(4\pi p^2)f_s(r, p, t)$, where $f_s(r, p, t)$ is the number density of particle species s of momentum p at radial position r , and time t in the phase space.

For CRPs, the FP equation can be written as (Nishiwaki et al. 2021)

$$\begin{aligned} \frac{\partial N_p}{\partial t} = & \frac{\partial}{\partial p} \left[N_p \left(b_C^{(p)} - \frac{1}{p^2} \frac{\partial}{\partial p} (p^2 D_{pp}) \right) \right] \\ & + \frac{\partial^2}{\partial p^2} [D_{pp} N_p] + \frac{\partial}{\partial r} \left[D_{rr} \frac{\partial N_p}{\partial r} - \frac{2}{r} N_p D_{rr} \right] \\ & + Q_p(r, p) - \frac{N_p}{\tau_{pp}(r, p)}, \end{aligned} \quad (1)$$

where $N_p^{\text{tot}}(r, p, t)$ is the distribution function of CRPs, $b_C^{(p)}$ is the momentum loss rate ($b \equiv -dp/dt$) due to the Coulomb collisions, D_{rr} and D_{pp} are the spatial and momentum diffusion coefficients due to interactions with turbulence, and $Q_p(r, p)$ denotes the injection of primary CRPs. The factor τ_{pp} denotes the pp collision timescale. For simplicity, we ignore the effect of repeated collisions of a CRP, so we do not follow an energy loss per collision. The cooling due to the pp collision is expressed like escape as $-N_p/\tau_{pp}$, where the loss timescale includes the inelasticity coefficient of $\kappa_{pp} = 0.5$. The details of τ_{pp} , $b_C^{(p)}$, and D_{rr} are shown in Nishiwaki et al. (2021).

For CREs, the FP equation is expressed as

$$\begin{aligned} \frac{\partial N_e}{\partial t} = & \frac{\partial}{\partial p} \left[N_e \left(b_{\text{rad}} + b_C^{(e)} - \frac{1}{p^2} \frac{\partial}{\partial p} (p^2 D_{pp}) \right) \right] \\ & + \frac{\partial^2}{\partial p^2} [D_{pp} N_e] + \frac{\partial}{\partial r} \left[D_{rr} \frac{\partial N_e}{\partial r} - \frac{2}{r} N_e D_{rr} \right] \\ & + Q_e(r, p; N_p), \end{aligned} \quad (2)$$

where $b_C^{(e)}$ is the energy loss rate due to CRE-e collisions, b_{rad} denotes the radiative cooling, and $Q_e(r, p; N_p)$ is the source term, which includes both the secondary

and primary injections: $Q_e(r, p; N_p) = Q_e^{\text{sec}}(r, p; N_p) + Q_e^{\text{pri}}(r, p)$. We use the same formulae for the momentum loss term b , $b_C^{(e)}$ and b as those given in Nishiwaki et al. (2021). We do not solve the evolution of high-energy CREs of $p > 10^7 m_e c$ to save the computation time.

The radial profile of the thermal electron density is expressed with the beta-model profile as

$$n_{\text{th}}(r) = n_{\text{th}}(0) \left\{ 1 + \left(\frac{r}{r_c} \right)^2 \right\}^{-\frac{3}{2}\beta}. \quad (3)$$

The parameters for the Coma cluster are (Briel et al. 1992), $n_{\text{th}}(0) = 3.42 \times 10^{-3} \text{cm}^{-3}$, $\beta = 0.75$, and $r_c = 290$ kpc. We also use the same temperature profile as that in Nishiwaki et al. (2021). For simplicity, the ICM is a pure hydrogen plasma, and we use Eq. (3) for the density of thermal protons in our model.

Relativistic electrons can be produced through the decay of pions produced by the inelastic collisions between CRPs and thermal protons ($p+p \rightarrow \pi^{0,\pm} + X$). We adopt the same method as that in Nishiwaki et al. (2021) to calculate the secondary injection from pp collisions.

2.2. Injection of primary cosmic-rays

Primary CRPs can be accelerated through the shocks caused by the structure formation process or injected in the ICM from the internal sources like AGNs. We assume a single power-law spectrum with an exponential cutoff for the injection spectrum of primary CRs;

$$Q_p(r, p) = C_p^{\text{inj}} p^{-\alpha_{\text{inj}}} \exp \left[-\frac{E_p}{E_p^{\text{max}}} \right] \mathcal{Q}(r), \quad (4)$$

where C_p^{inj} is the normalization factor, and $\mathcal{Q}(r)$ represents the radial dependence of the injection¹. Those two quantities can be constrained by the observed flux and the brightness profile of the RH, respectively. The maximum energy of primary CRPs is taken to be $E_p^{\text{max}} = 100$ PeV. The minimum momentum of CRPs is taken to be ten times larger than that of the thermal protons. Following Brunetti et al. (2017), we adopt the injection index of $\alpha_{\text{inj}} = 2.45$.

We also take into account the injection of primary CREs. The number ratio of primary CREs to primary CRPs at the injection is expressed with a parameter f_{ep} ;

$$Q_e^{\text{pri}}(r, p) = f_{\text{ep}} Q_p(r, p). \quad (5)$$

Eq. (4), which is defined only above the minimum momentum of CRPs, $p = 30 \text{ MeV}/c$, is extrapolated to

¹ $\mathcal{Q}(r)$ is equivalent to $K(r)$ in Nishiwaki et al. (2021)

the minimum momentum of CREs, $p_e = 0.3m_e c = 150$ keV/c, where the strong Coulomb cooling inhibits the reacceleration.

As we have mentioned, we compare the two scenarios: the secondary scenario ($f_{\text{ep}} = 0$), where all of CREs are produced through the pp collision, and the primary scenario ($f_{\text{ep}} = 0.01$), where the primary CRE injection dominates the injection from the hadronic interaction. The adopted ratio of $f_{\text{ep}} = 0.01$ is close to the observed CRE to CRP ratio in our galaxy (e.g., [Schlickeiser 2002](#)). We neglect the possible radial dependence of f_{ep} (e.g., [Pfrommer et al. 2008](#)) for simplicity. In Sect. 3, we show that the expected lifetime of the radio emission is significantly different between these two scenarios.

The extended profile of RHs indicates a fair amount of CREs outside the thermal core of the cluster. This challenges the secondary scenario, since the injection of secondary CREs is more effective at smaller radii where the timescale of the pp interaction is shorter. [Nishiwaki et al. \(2021\)](#) tested the case where the injection profile $K(r)$ has a peak at $r \approx 1$ Mpc to reproduce the surface brightness profile of the Coma RH. However, even though CRPs are injected outside the core, high-energy CRPs selectively diffuse into the core, where the radio emissivity is higher due to the stronger magnetic field. As a result, the spectral hardening is caused by this radial diffusion of parental CRPs, and this makes it difficult to fit the observed spectrum. This difficulty is expected to be relaxed if the reacceleration is more efficient at larger radii.

In this paper, we assume that CRs in the ICM are mainly injected from internal sources, such as AGN activities and other outflows from member galaxies. We adopt the injection profile of primary CRs proportional to the thermal density profile (Eq. (3)):

$$\mathcal{Q}(r) = \left\{ 1 + \left(\frac{r}{r_c} \right)^2 \right\}^{-\frac{3}{2}\beta}, \quad (6)$$

where we use the same r_c and β as Eq. (3). We fix this injection for both the primary and secondary scenarios. As will be explained in Sect. 2.3, the observed brightness profile of the RH can be modeled by tuning the radial profile of D_{pp} .

2.3. Reacceleration and spatial diffusion

Recent studies show that the observed \sim Mpc extension of the Coma RH with the cored profile of the magnetic field ([Bonafede et al. 2010](#)) requires the CR profile flatter than the ICM profile (e.g., [Brunetti et al. 2017](#); [Pinzke et al. 2017](#)). In this study, we consider that the extended profile of radio-emitting CREs is reproduced

by the radial dependence of the reacceleration coefficient, D_{pp} , rather than that of the CR injection. This assumption is supported by the turbulent profile often seen in the numerical simulations of the cluster formation (e.g., [Nelson et al. 2014](#); [Vazza et al. 2017](#); [Angelinelli et al. 2020](#)). In the following, we discuss how the profile of D_{pp} is related to the profile of the turbulence, using the expression derived from the quasi-linear theory. As a result, $D_{pp}(r, p)$ will be expressed with two parameters; one is for the radial dependence, and the other is for the normalization.

A merger of two clusters would cause a turbulent motion with a typical velocity of $V_L \sim 10^3$ km/s at the scale of the core radius of the ICM ($L \sim 500$ kpc) (e.g., [Brunetti & Lazarian 2007](#)). A part of the turbulent energy can be transferred into CRs through stochastic wave-particle interactions. We assume that the (re)acceleration of CRs occurs through the transit-time damping (TTD) with the compressible turbulence in the ICM (e.g., [Brunetti & Lazarian 2007](#)). In this case, the momentum diffusion coefficient becomes hard-sphere type ($D_{pp} \propto p^2$), which implies that the acceleration timescale is independent of the particle momentum $t_{\text{acc}} = p^2/(4D_{pp}) \propto p^0$.

We assume that the fast mode turbulence in the ICM is well described with the Iroshnikov-Kraichnan (IK) scaling (e.g., [Brunetti & Lazarian 2011](#)). Isotropic cascades of fast mode turbulences with the IK spectrum are seen in numerical simulations (e.g., [Cho & Lazarian 2003](#)). Then, the energy spectrum of the turbulence per unit mass $\mathcal{W}(k)$ at wavenumber k is written as

$$\rho \mathcal{W}(k) = \sqrt{\frac{2}{7}} I_L \rho c_s k^{-3/2}, \quad (7)$$

where ρ and c_s are the mass density and sound velocity of the ICM, respectively, and I_L is the volumetric energy injection rate ([erg/cm³/s] in c.g.s unit). Most of the turbulent energy is stored in the outer scale $k_L \mathcal{W}(k_L) \approx V_L^2$,

This means that I_L and k_L are related as

$$I_L \approx \frac{7}{2} \rho \frac{V_L^4}{c_s} k_L, \quad (8)$$

Using the above turbulent energy spectrum, D_{pp} can be written as (e.g., [Miniati 2015](#))

$$D_{pp}(r, p) = \frac{p^2 \pi I_\theta(x)}{8c} \int_{k_L}^{k_{\text{cut}}} dk k \mathcal{W}(k), \quad (9)$$

where k_L corresponds to the injection scale. Here, we assumed that the turbulence is isotropic with respect to the background magnetic field. The average over the

angle θ between the direction of the wave and the background magnetic field is represented by a dimensionless function, $I_\theta(x) \equiv \int_0^{\arccos(x)} d\theta \frac{\sin^3 \theta}{|\cos \theta|} \left[1 - \left(\frac{x}{\cos \theta} \right)^2 \right] \approx 5$, where $x = v_{\text{ph}}/c$ and v_{ph} is the phase velocity of the wave. Because the TTD is the interaction with the fast mode waves and the ICM is a high-beta plasma ($\beta_{\text{pl}} \gtrsim 100$ for $\sim 1\mu\text{G}$ magnetic field), we adopt the sound velocity c_s for v_{ph} .

We have assumed that the turbulence is damped at the cut-off scale, k_{cut} , where the damping timescale becomes comparable to the cascade timescale. When the wave damping of the turbulence is dominated by the TTD interaction with thermal electrons, the damping rate averaged over the angle between the wave and the background magnetic field, θ , can be approximated as (Miniati 2015),

$$\langle \Gamma_{\text{TTD}} \rangle_\theta = \left(\frac{3\pi m_e}{20m_p} \right)^{\frac{1}{2}} \left\langle \frac{\sin^2 \theta}{\cos \theta} e^{-\frac{5m_e}{3m_p \cos^2 \theta}} \right\rangle_\theta c_s k, \quad (10)$$

where $\langle \rangle_\theta$ represents the angle average. Here, we have used the relation, $\beta_{\text{pl}} |B_k|^2 / 16\pi \sim \rho \mathcal{W}(k)$, for the perturbed magnetic field B_k at wavenumber k .

Equating with the cascade rate for the IK spectrum, the cut-off scale is approximated as $k_{\text{cut}} \approx 6.75 \times 10^2 \left(\frac{\mathcal{M}_s}{0.5} \right)^4 k_L$, where $\mathcal{M}_s = V_L/c_s$ is the Mach number for the turbulent velocity at the injection scale (Brunetti & Lazarian 2007).

The diffusion coefficient D_{pp} could depend on the radial coordinate r through the profile of the turbulent energy density. Instead of specifying the parameters such as I_L and k_L at each radius, we use another parameter, $t_{\text{acc}}(r_c)$, that represents the acceleration timescale at $r = r_c$, and discuss constraints on this parameter from the observed spectrum. Introducing cut-off factors for both the maximum and the minimum energies (Nishiwaki et al. 2021), the diffusion coefficient may be written as

$$D_{pp}(r, p) = \mathcal{D}(r) \frac{p^2}{4t_{\text{acc}}(r_c)} \times \exp \left[-\frac{E(p)}{E_c^{\text{max}}(r)} \right] \exp \left(-\frac{m_s c}{p} \right), \quad (11)$$

where $\mathcal{D}(r)$ is a dimensionless factor representing the radial dependence, and m_s is the mass of particle species s . We adopt the Hillas limit (Hillas 1984) for the maximum energy of CRs, $E_c^{\text{max}}(r) = qB(r)l_c^{\text{F}} \sim 9 \times 10^{19} (B(r)/1 \mu\text{G}) (l_c^{\text{F}}/0.1\text{Mpc}) \text{ eV}$, where l_c^{F} is the maximum size of the turbulent eddy of compressible turbulence. We assume $l_c^{\text{F}} = 0.1 \text{ Mpc}$ as a reference, which is compatible with the constraint from the thermal Sunyaev-Zel'dovich effect (SZ) observation of the Coma cluster (Churazov et al. 2012).

Following Pinzke et al. (2017), we introduce a radial dependence of the volumetric injection rate of turbulence energy, $I_L(r)$. We assume that $I_L(r)$ is a power-law function of the thermal energy density ε_{th} with a cut-off on a spatial scale as

$$I_L(r) \propto \varepsilon_{\text{th}}^{\alpha_{\text{turb}}}(r) \exp \left[-\left(\frac{r}{R_{500}} \right) \right], \quad (12)$$

where R_{500} is a parameter R_Δ with $\Delta = 500$. The radius R_Δ is defined as the radius inside which the average of the total density ρ_{tot} becomes Δ times the critical density of the Universe, ρ_{cr} :

$$R_\Delta = \left[\frac{3M_\Delta}{4\pi\Delta\rho_{\text{cr}}(z)} \right]^{1/3}, \quad (13)$$

$$M_\Delta = \int_0^{R_\Delta} dr 4\pi r^2 \rho_{\text{tot}}(r). \quad (14)$$

We adopt $R_{500} = 47 \text{ arcmin}$ for the Coma cluster (Planck Collaboration et al. 2013), which corresponds to $R_{500} = 1.35 \text{ Mpc}$ under the cosmology we adopted. The need for the cut-off in Eq. (12) is discussed in Section 2.5. In this model, the energy density ratio of the turbulence to the thermal gas becomes

$$\frac{\varepsilon_{\text{turb}}}{\varepsilon_{\text{th}}} \propto \varepsilon_{\text{th}}^{\frac{\alpha_{\text{turb}}-1}{2}}(r) T^{-\frac{1}{4}}(r) \exp \left[-\left(\frac{r}{R_{500}} \right)^{\frac{1}{2}} \right]. \quad (15)$$

From Eqs. (9) and (7), we obtain $D_{pp}(r, p) \propto \mathcal{M}_s^4 c_s k_L \propto \frac{c_s(r)}{c} \frac{I_L(r)}{\rho(r)c_s^2(r)}$. For simplicity, the injection scale k_L is assumed to be a constant. With those assumptions concerning I_L and k_L , the radial dependence factor $\mathcal{D}(r)$ in Eq. (11) can be expressed with one parameter, α_{turb} :

$$\mathcal{D}(r) = \mathcal{D}_0 \varepsilon_{\text{th}}^{\alpha_{\text{turb}}-1}(r) \sqrt{T_e(r)} \exp \left[-\left(\frac{r}{R_{500}} \right) \right], \quad (16)$$

where the normalization is given at $r = r_c$, i.e., $\mathcal{D}_0^{-1} = \varepsilon_{\text{th}}^{\alpha_{\text{turb}}-1}(r_c) \sqrt{T_e(r_c)} \exp \left[-\left(\frac{r_c}{R_{500}} \right) \right]$.

Using Eqs. (7)-(9) and neglecting the cut-off terms in Eq. (11), $t_{\text{acc}}(r_c)$ can be obtained as a function of the ratio of the turbulent energy density, $\epsilon_{\text{turb}} \approx \rho V_L^2$, to the thermal energy density:

$$t_{\text{acc}}(r) \approx 300 \text{ Myr} \left(\frac{\epsilon_{\text{turb}}/\epsilon_{\text{th}}(r)}{0.5} \right)^{-2} \left(\frac{L}{500 \text{ kpc}} \right)^{-1} \times \left(\frac{I_\theta(x)}{0.5} \right)^{-1} \left(\frac{c_s(r)}{10^3 \text{ km/s}} \right)^{-2} \quad (17)$$

where $x = c_s(r)/c$.

As for the spatial diffusion of CRs in the ICM, we assume that the isotropic pitch angle scattering with

Alfvén waves plays a dominant role. We adopt the Kolmogorov scaling for the Alfvénic turbulence (e.g., [Cho & Lazarian 2003](#)) down to the Larmor scale of CRs with GeV energies. Unlike the compressible turbulence, which is injected through major mergers and can be the agent for the TTD acceleration, incompressible Alfvén waves can exist in the ICM over the cluster lifetime, supported by a constant injection through frequent minor mergers.

We neglect the possible radial dependence in the Alfvénic turbulence and adopt the same D_{rr} as assumed in [Nishiwaki et al. \(2021\)](#). We rather focus on the relation between the observed brightness profile and the r -dependence in D_{pp} . Note that the radial diffusion of CRs below ≈ 10 GeV is almost negligible, as long as D_{rr} has a similar value to the one in [Nishiwaki et al. \(2021\)](#). Since the typical energy of parent CRPs for the GeV CREs is 10 GeV, the effect of the radial diffusion is marginal even in the secondary scenario.

2.4. Model outline

In our modeling, the history of the RH evolution is divided into following three phases:

- *Injection phase.* In this phase, we follow the long-term evolution of the CR distribution before the major merger event. We integrate the FP equations (Eqs. (1) and (2)) with $D_{pp} \equiv 0$ for 4 Gyr until the CRE spectrum settles in a steady shape due to the balance between the constant injection and the cooling processes.
- *Reacceleration phase.* This phase starts just after a major merger event. The merger-induced turbulence reaccelerates CRs. The initial condition of this phase is the final state of the injection phase. We follow the evolution including the reacceleration expressed with the diffusion coefficient of Eq. (11). The Coma RH is assumed to be in this phase and the elapsed time in this phase, t_R , is treated as a model parameter. We do not consider the time evolution of the turbulence, so the parameters, α_{turb} and t_{acc} are not time dependent.
- *Cooling phase.* After the reacceleration ceases, the emission decays with time. This phase is modeled with $D_{pp} = 0$, and the emission lifetime will be investigated in Section 3.

The CR injection spectral index is fixed to be $\alpha_{\text{inj}} = 2.45$, which can model the typical radio spectral index of RHs, $\alpha_{\text{syn}} \approx 1.2$. Concerning the CR injection, we have one free parameter, L_p^{inj} , which is the injection luminosity (in unit of [erg/s]) of relativistic ($p > m_p c$)

protons integrated over the cluster volume, i.e., $L_p^{\text{inj}} = \int dr \int dp E_p(p) Q_p(r, p)$, where $E_p(p) = \sqrt{m_p^2 c^4 + p^2 c^2}$. The injection rate of primary CREs is determined by Eq (5).

For a given magnetic field, our model includes four parameters: the CR injection luminosity, L_p^{inj} , the power-law index for the radial dependence of D_{pp} , α_{turb} , the timescale of the reacceleration at a given radius, $t_{\text{acc}}(r_c)$, and the elapsed time after the reacceleration onset, t_R .

2.5. Modeling the Coma RH

In this section, we apply the model explained above to the Coma RH and discuss the constraints on the model parameters. The radial dependence of D_{pp} is constrained by the observed brightness profile, while t_R , t_{acc} , and L_p^{inj} are by the spectral shape and the flux at a given frequency. With those parameters, we study the emission lifetime in Section 3.

The magnetic field in the Coma cluster is well studied with the rotation measure (RM) measurements. Here we use the following scaling of the magnetic field strength with cluster thermal density:

$$B(r) = B_0 \left(\frac{n_{\text{th}}(r)}{n_{\text{th}}(0)} \right)^{\eta_B}, \quad (18)$$

where the best fit values are $B_0 = 4.7 \mu\text{G}$ and $\eta_B = 0.5$ ([Bonafede et al. 2010](#)), and see Eq. (3) for $n_{\text{th}}(r)$. The uncertainty in the magnetic field and its impact on the multi-wavelength spectrum are discussed in [Nishiwaki et al. \(2021\)](#).

For a fixed injection of primary CRPs, the profile of the turbulence α_{turb} can be constrained from the brightness profile of the RH. Before the reacceleration, the injection with profile of Eq. (4) produces too steep brightness profile in both primary and secondary scenarios (dashed lines in Figure 1). This steepness is further enhanced in the secondary model because of the density dependence of the electron injection.

As seen from Eq. (11), the turbulent profile with $\alpha_{\text{turb}} < 1$ enhances the acceleration at larger radii ($r > r_c$), and the brightness profile would be modified to fit the observation. As shown in Figure 1, we find that $\alpha_{\text{turb}} = 0.28$ and $\alpha_{\text{turb}} = 0.52$ provide the best fit to the secondary and the primary scenarios, respectively. The other model parameters are summarized in Table 1. The radial dependence of the acceleration timescale $t_{\text{acc}}(r) \equiv p^2 / (4D_{pp}(r, p))$ is shown in Figure 2. Adopting Eq. (17) with constant $L = 500$ kpc, we estimate the turbulent energy density from t_{acc} as shown in Figure 2.

In the secondary scenario, the reacceleration timescale at the edge of the RH is required to be almost 2 times shorter than inside the core region. The decline of t_{acc}

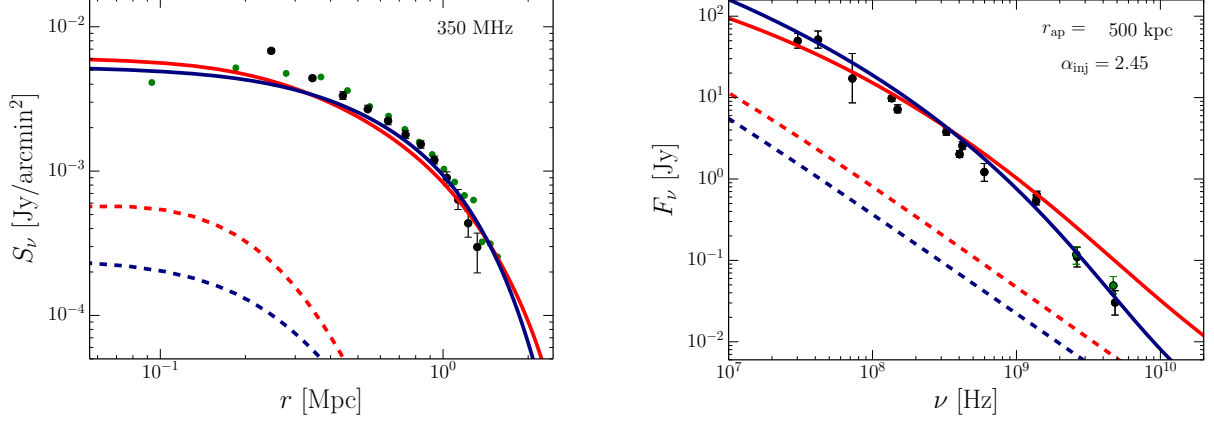


Figure 1. Left panel: Brightness profile of the Coma RH at 350 MHz. Right panel: The spectrum is calculated by integrating the intensity within the aperture radius of $r_{\text{ap}} = 500$ kpc. The results for secondary and primary scenarios are shown with red and blue lines, respectively. The dashed lines show the emission before the reacceleration. Data points are taken from Pizzo (2010); Pinzke et al. (2017); Brunetti et al. (2017).

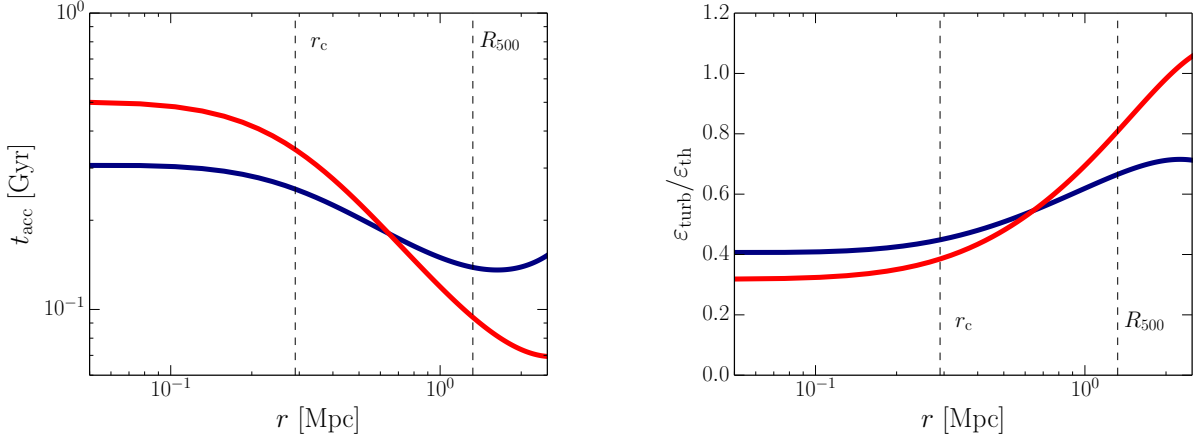


Figure 2. Radial profile of t_{acc} (Left) and $\epsilon_{\text{turb}}/\epsilon_{\text{th}}$ (Right) in the same models in Fig. 1. The red and blue lines show results of the secondary ($\alpha_{\text{turb}} = 0.28$) and the primary ($\alpha_{\text{turb}} = 0.52$) scenarios, respectively. The turbulent energy density is calculated from Eq. (17) with $L = 500$ kpc. The vertical dashed lines show the radius correspond to r_c and R_{500} of the Coma cluster.

towards large radii is suppressed by the artificial cut-off of the turbulent profile at R_{500} (Eq. (16)), with which the observed decline of the brightness around 1 Mpc is well explained.

If we omit the cut-off term in Eq. (16), the acceleration efficiency becomes unrealistically high at the periphery of the cluster. Although a model without the cutoff can explain the synchrotron spectrum within $r_{\text{ap}} = 500$ kpc, the gamma-ray flux calculated within $r < R_{200}$ exceeds the upper-limit given by Fermi-LAT (Ackermann et al. 2016) in the secondary scenario. This problem can be circumvented by introducing the cut-off. In our fiducial secondary model shown in Figure 2, the turbulent energy dominates the thermal energy at large radii.

The elapsed time, t_R , and the timescale of reacceleration, t_{acc} , can be constrained from the spectral shape

of the RH (see Nishiwaki et al. 2021, for the detail), especially the spectral steepening around 1 GHz. We find that $t_{\text{acc}}(r_c) \approx 300$ Myr is favorable in both the scenarios.

In Nishiwaki et al. (2021), we have shown that the combination of the reacceleration and spatial diffusion of CRPs enhances the production of secondary CREs at higher energies, when the primary accelerator is located at the periphery of the RH. This causes a spectral hardening in the CRE distribution. A softer spectrum would be expected when the injection is more concentrated towards the cluster center, since that reduces the effect of energy-dependent radial diffusion. However, we find that this effect is not so strong compared to the spectral hardening due to the log-scaling in the cross section of the pp collision (e.g., Kamae et al. 2006), and our sec-

ondary model still predicts a larger flux above 1 GHz (Figure 1).

A possible prescription for that tension is adopting a steeper injection index. The spectra for different α_{inj} are shown in Appendix A, where we change $L_{\text{p}}^{\text{inj}}$ and t_{R} for each α_{inj} to fit the data, while the other parameters, α_{turb} and t_{acc} are fixed. We find that the $\alpha_{\text{inj}} = 3.0$ model provides a better fit to the higher frequencies. Since the purpose of this paper is the discussion about the RH statistics, we do not excessively tune the parameters to match with the Coma RH spectrum. Throughout this paper, we fix $\alpha_{\text{inj}} = 2.45$ as a fiducial value (e.g., Pinzke & Pfrommer 2010; Brunetti et al. 2017).

In each scenario, The expected flux of gamma-ray becomes smaller than the upper limit by Fermi-LAT observation (Ackermann et al. 2016). Note that possible gamma-ray signals are reported in the direction of Coma (e.g., Xi et al. 2018; Adam et al. 2021). The predicted flux in our secondary scenario is comparable to the data reported in those papers, while the GeV gamma-ray flux becomes almost two order of magnitude lower in the primary model.

Table 1. Model parameters for the Coma radio halo

model	α_{turb}	t_{acc} (at $r = r_c$) [Myr]	t_{R} [Myr]	$L_{\text{p}}^{\text{inj}}$ [erg s ⁻¹]
secondary	0.28	330	340	9.3×10^{43}
primary	0.52	255	300	7.3×10^{42}

NOTE—The other fixed parameters are 4 Gyr for the duration of the injection phase, $\alpha_{\text{inj}} = 2.45$ for the slope of the injection spectrum, and the cutoff R_{500} of the turbulent profile.

As shown in Table 1, the acceleration timescale t_{acc} are similar to those in the previous studies (e.g., Brunetti et al. 2017; Nishiwaki et al. 2021). However, the primary CR injection luminosity in the primary scenario is one order of magnitude larger than that in Nishiwaki et al. (2021). This is attributed to the different best fit values of $t_{\text{R}}/t_{\text{acc}}$. In our previous model, $t_{\text{R}}/t_{\text{acc}} \gtrsim 3.0$ is required to match the brightness at outer radii ($r > 500$ kpc), while this requirement is relaxed considering the radially increasing turbulent profile. The relatively small $t_{\text{R}}/t_{\text{acc}}$ in the current model reduces the energy contribution from the reacceleration, which in turn increases the contribution from the primary CR injection. The injection power of primary CREs ($p_{\text{ec}} \geq 150$ keV) is smaller than that of CRPs ($p_{\text{c}} \geq 30$ MeV) by a factor of ≈ 5 in the primary scenario with $\alpha_{\text{inj}} = 2.45$.

In our previous study, we modeled the brightness profile of Coma with a fine-tuned injection profile with larger number of model parameters, under the assumption of spatially homogeneous acceleration efficiency. In this study, however, we succeeded in the modeling with much simpler injection profile (Eq. (4)), adopting the turbulent profile shown in Figure 2. Note that both the models are compatible with the current radio observations. The direct measurement of turbulent velocity with future X-ray telescopes featured with improved spectral resolution and effective area is desired to distinguish those two models.

2.6. Comparison to *M-turbulence* Model

A similar turbulent profile for a Coma-like halo is obtained in Pinzke et al. (2017). They calculate the injection and propagation of seed CRs on Lagrangian particle trajectories as a post-process of cosmological hydrodynamical simulations. In their *M-turbulence* model, the same CRE-to-CRP ratio as our primary scenario, i.e., $f_{\text{ep}} = 0.01$, is adopted. The primary CRs are assumed to be injected via diffusive shock acceleration at shocks in the simulation. The acceleration efficiency is expressed as the function of the shock Mach number and the magnetic field strength of the down stream. They also assume the power-law scaling between I_L and ε_{th} without a cut-off: $I_L \propto \varepsilon_{\text{th}}^{\alpha_{\text{turb}}}$. The best-fit value for their *M-turbulence* model is $\alpha_{\text{turb}} = 0.67$, which is slightly larger than our primary scenario. The model in Pinzke et al. (2017) and our model are in very good agreement concerning the profile of t_{acc} , although the overall normalization is larger in their *M-turbulence* model by a factor ~ 2 .

3. LIFETIME OF RADIO HALOS

In this Section, we discuss the lifetime of RHs in the cooling phase (Section 2.4). As an example case, we present the time evolution of a Coma-like cluster after the reacceleration ends. In this cooling phase, we solve the FP equation with $D_{pp} = 0$. In our method, we do not follow the evolution of the turbulent spectrum, so the acceleration timescale is assumed to be constant within the reacceleration phase and it suddenly turns to be zero at the transition to the cooling phase. Three competing effects govern the evolution of the CR spectra: cooling processes, injections (primary and secondary), and spatial diffusion. Concerning CREs, the effect of the spatial diffusion is negligible because of the short cooling timescale.

The model is basically the same as that explained in Section 2. We adopt the same magnetic field, ICM profile, CR injection profile, slope of the injection spectrum,

and redshift. We adopt the model parameters, such as L_p^{inj} , t_{acc} , and α_{turb} , from the obtained values in Section 2. However, we change t_R as explained in the following.

The initial condition for the cooling phase corresponds to the final state of the reacceleration phase. To set the initial condition, the maximum duration of the reacceleration phase needs to be specified. In the case of the Coma RH, the present stage does not necessarily correspond to the end of the reacceleration phase, i.e., the peak of the luminosity evolution. We assume that the Coma RH is in the midst of the reacceleration phase. Considering that there exist some RHs with masses similar to the mass of Coma and much brighter radio luminosities as $P_{1.4} \approx 10^{25}$ W/Hz, such as RXCJ 0510.7-0801 and Abell 2744 (Cuciti et al. 2021b), we assume that a Coma-like cluster could achieve similar luminosity at $t_R = t_R^{\text{peak}}$. Our model suggests that the luminosity of a Coma-like halo reaches that value around $t_R \approx 500$ Myr (about 200 Myrs from the present stage of Coma). Thus, we set the initial condition for the cooling phase by the state at $t_R^{\text{peak}} = 500$ Myr.

In the following, we compare the two scenarios for the seed population: the secondary scenario (Section 3.1) and the primary scenario (Section 3.2). We define the emission lifetime as the duration for which the flux at 1.4 GHz, $F_{1.4}$, satisfies the condition, $F_{1.4} \gtrsim 0.1 F_{1.4}^{\text{peak}}$, where $F_{1.4}^{\text{peak}}$ is its peak value.

3.1. Secondary scenario

In the left panel of Figure 3, we show the time evolution of synchrotron spectrum of our Coma-like cluster in the secondary scenario. We adopt the model parameters, $\alpha_{\text{turb}} = 0.28$, $t_{\text{acc}} = 330$ Myr (at $r = r_c$), and $t_R = 500$ Myr. The aperture radius is fixed to $r_{\text{ap}} = 500$ kpc. The thick black line shows the flux at the end of the reacceleration phase, or the beginning of the cooling phase. The flux at each epoch in the cooling phase is distinguished by colors, as it evolves from red to blue. After several 100 Myrs, the spectrum approaches a power-law shape due to the balance between the electron injection and the cooling. The flux decrement in the cooling phase is at most one order of magnitude and most highlighted at ≈ 300 MHz, where the cooling and acceleration balance in the reacceleration phase. At higher frequencies ($\nu > 1$ GHz), the peak flux is maintained by a high injection rate of secondary CREs from reaccelerated CRPs. Since parent CRPs do not significantly suffer from cooling, the flux at > 1 GHz is maintained even after the reacceleration phase. Therefore, the lifetime of the RH can be much

longer than the cooling time of CREs especially at high frequencies.

Our calculation demonstrates that not only the reacceleration of the pre-deposited secondary CREs but also the fresh electrons injected from reaccelerated CRPs make significant contributions to the radio emission. The fractional contribution of those two components could depend on the parameters, t_{acc} and t_R^{peak} . As shown in Nishiwaki et al. (2021), in the reacceleration phase, the evolution of the radio flux around 300 MHz is relatively faster than that of the gamma-ray flux originated from π^0 decay. This suggests that as t_R/t_{acc} increases, in the radio flux, the contribution of the reaccelerated CREs dominates that of the enhanced electron injection from reaccelerated CRPs. Even at 1.4 GHz, the flux decay would be more prominent, if the reacceleration is more efficient ($t_{\text{acc}} \ll 200$ Myr) or the reacceleration lasts longer ($t_R^{\text{peak}} \gg 500$ Myr). However, such a model causes a tension with the observed spectral feature of the Coma RH (e.g., Nishiwaki et al. 2021) or the radio luminosity becomes far brighter than any observed RHs.

Note that such long-living emission is achieved only under the assumption of hard-sphere type reacceleration ($D_{pp} \propto p^2$), where the reacceleration timescale is the same between CRPs and CREs. When the CRP reacceleration is less efficient compared to that for CREs, e.g., in the case of the Kolmogorov type reacceleration (Nishiwaki et al. 2021), the emission would decline within a few times the cooling timescale.

As the radiative cooling proceeds, the shape of the spectrum approaches to a single power-law shape. The concave shape caused by the reacceleration disappears within a few times the cooling timescale. If the observed break feature around 1.4 GHz is considered to be significant, the RH in Coma should still be in the reacceleration phase or within ≈ 200 Myrs after the reacceleration stops.

In Figure 4, we show the evolution of the brightness profile at 350 MHz. The decline of the brightness is within one order of magnitude, consistent with the spectral evolution. Given a threshold for S_ν , the size of the RH shrinks with time. For example, considering an observational threshold around $S_\nu \approx 10^{-2}$ [Jy/arcmin²], the apparent RH size evolves from 1 Mpc to 0.5 Mpc in the cooling phase. A slight increase of the brightness in the core region is seen at the later stage. This is a transitional phenomenon while the CRE distribution is evolving towards the equilibrium state regulated by the balance between the cooling and the enhanced injection from reaccelerated CRPs.

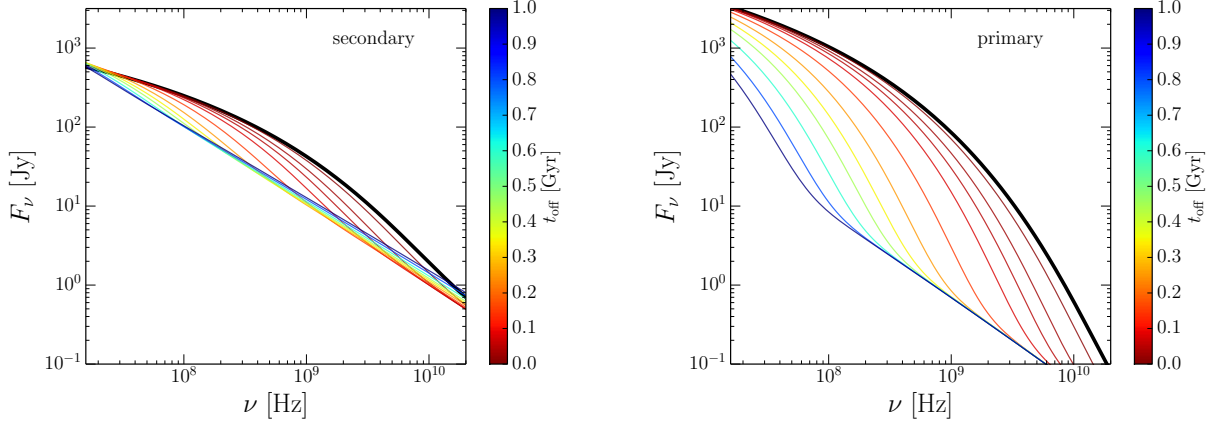


Figure 3. Time evolutions of the synchrotron flux of a Coma-like RH at the cooling phase in the secondary (Left) and primary (Right) scenarios. The elapsed time (distinguished with different colors) is measured from the peak time, which corresponds to the time when the reacceleration ends. The thick black line shows the spectrum at the peak time.

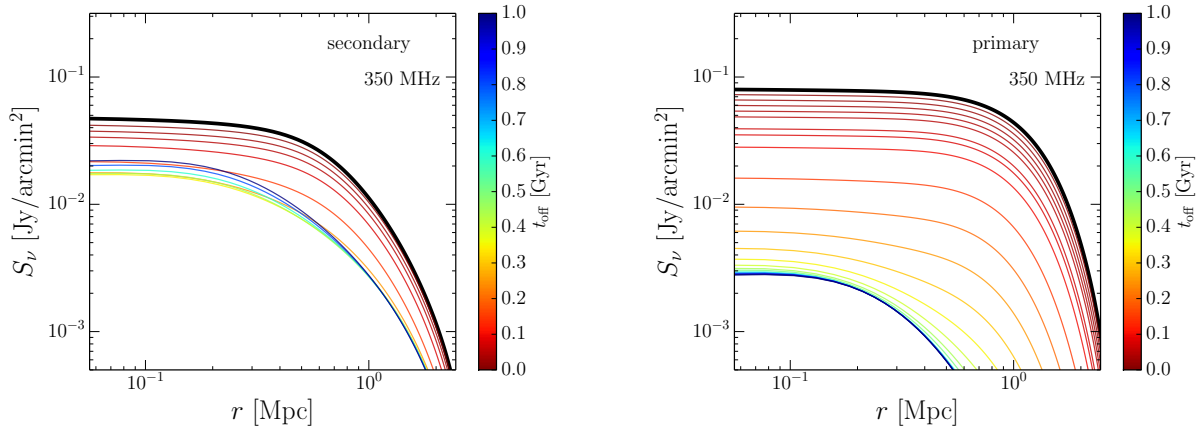


Figure 4. Time evolution of the brightness profile of a Coma-like RH at 350 MHz in the cooling phase. The color code is the same as that in Figure 3.

3.2. Primary scenario

The right panel of Figure 3 shows the spectral evolution in the primary scenario. The model parameters are, $\alpha_{\text{turb}} = 0.52$, $t_{\text{acc}} = 255$ Myr (at $r = r_c$), and $t_R = 500$ Myr. In this case, the evolution of the secondary injection rate is negligible, and the radio flux in lower frequencies ($\nu < 1$ GHz) decays almost one order of magnitude within ≈ 500 Myr after the end of the reacceleration phase. The lifetime of the RH at 1.4 GHz is comparable to the cooling timescale of responsible electrons, or the reacceleration timescale, as shown in the previous studies (Cassano & Brunetti 2005).

The evolution of the brightness profile is shown in the right panel of Figure 4. Adopting the same threshold for S_ν as in Sect. 3.1, we find that the RH disappear in 400 Myr after the peak time. In this scenario, not only the flux but also the size of the RH show rapid increase and decrease. Considering both the reacceleration phase

and the cooling phase, one can approximate the lifetime of the giant RH as ≈ 500 Myr in total.

The spectral profile at the late stage of the cooling phase, $t_{\text{off}} > 1$ Gyr, is not equivalent to the pre-reacceleration profile (Figure 1 dashed line). This difference is originated from the assumption of $f_{\text{ep}} = 0.01$, i.e., the finite injection rate of CRPs even in the primary scenario. The off-state emission is supported by the enhanced injection from reaccelerated CRPs, although the synchrotron flux becomes smaller by one order of magnitude than the peak state.

3.3. Discussion

In this Section, we have discussed the lifetime of the radio emission around 1.4 GHz. As seen from Figure 3, the lifetime depends on the frequency. A longer time is required for lower frequencies to reach the steady flux due to the balance between the cooling and the injection. In addition, the cooling timescale depends on the

magnetic field and redshift. Especially for the primary scenario, one can expect a much longer lifetime for a weaker magnetic field and lower frequencies.

While we have adopted $\alpha_{\text{inj}} = 2.45$, as demonstrated in Figure 7 in Nishiwaki et al. (2021), a smaller α_{inj} in the secondary model results in a harder and brighter flux around 10 GHz, where the emission is mostly powered by the injection from reaccelerated CRPs. Then, the decay of the emission seen in secondary scenario (Figure 3 left) becomes less important when $\alpha_{\text{inj}} < 2.45$.

We have estimated the RH lifetime under the “step-function approximation” for D_{pp} . In reality, the transition into the cooling phase would be gradual. If its transition timescale is much longer than the cooling timescale, the lifetime in the primary scenario can be longer than our estimate in the previous section.

4. MERGER TREE OF DARK MATTER HALOS

In the previous section, we have studied the lifetime of RHs. Our next steps is to calculate the population of RHs induced by cluster mergers, which can be compared with the observed statistic of RHs. In this Section, we explain our method to follow the cosmological evolution of galaxy clusters by constructing merger trees.

Merger trees describe the mass evolution of a dark matter (DM) halo. In the extended Press-Schechter (EPS) formalism (e.g., Press & Schechter 1974; Bond et al. 1991; Lacey & Cole 1993), the mass growth rate of a halo, or the conditional mass function, is given consistently with the Press-Schechter (PS) mass function. However, the EPS formalism tends to underestimate the number density of massive halos compared to cosmological N-body simulations (e.g., Sheth & Tormen 1999; Tinker et al. 2008). We introduce a Monte Carlo algorithm to build the merger trees compatible with the mass function given in those simulations.

4.1. Mean merger rate per halo

In our picture, DM halos evolve through stochastic mergers and continuous accretion of matters. Each halo experiences both the continuous mass evolution due to the accretion and the sudden mass increase due to the mergers. We employ the fitting formulae for the merger rate and the mass accretion rate (MAR) from N-body simulations (Fakhouri et al. 2010). However, as explained in the following, the separation between accretion and mergers is not definitive, so we need to define the minimum mass ratio for mergers, on which the estimate of the continuous mass accretion depends.

We treat a merger as a two-body event. The merger between $n \geq 3$ halos can be regarded as a sequence of binary mergers within a sufficiently small time interval.

For a merger between two halos of masses M_1 and M_2 , we call these two halos “progenitor” halos, and the one produced by the event “descendant” halo.

We use the dimensionless merger rate per descendant halo given by Fakhouri et al. (2010);

$$\frac{dN_m}{d\xi dz}(M_0, \xi, z) = A \left(\frac{M_0}{10^{12} \text{ M}_\odot} \right)^{k_1} \xi^{k_2} \exp \left[\left(\frac{\xi}{\tilde{\xi}} \right)^{k_3} \right] \times (1+z)^{k_4}, \quad (19)$$

where $M_0 = M_1 + M_2$ is the mass of a descendant halo, $\xi = M_2/M_1 \leq 1$ is the progenitor mass ratio, and the best fit parameters are $(k_1, k_2, k_3, k_4) = (0.133, -1.995, 0.263, 0.0993)$ and $(A, \tilde{\xi}) = (0.0104, 9.72 \times 10^{-3})$.

This expression diverges at $\xi = 0$, so we introduce a parameter, ξ_{min} , below which such frequent minor mergers are treated as a continuous accretion.

In the following sections, we assume that RHs are induced by “mergers” and discuss the condition for the RH onset. Thus, the value of ξ_{min} needs to be smaller than the threshold mass ratio for the RH onset, ξ_{RH} (Section 5.1). In this paper, we set $\xi_{\text{min}} = 10^{-3}$ to make the above condition satisfied with saving the computational cost. This value is larger than the minimum ξ used in Fakhouri et al. (2010). The number of mergers for given intervals Δz and $\Delta \xi$ is expressed as

$$\mathcal{P}(M_0, \xi, z) = \frac{dN_m}{d\xi dz} \Delta \xi \Delta z. \quad (20)$$

In our computation, we adopt sufficiently small values for Δz and $\Delta \xi$ so that $\mathcal{P}(M_0, \xi, z) < 10^{-3}$ for $\xi \geq \xi_{\text{min}}$, ensuring the two-body merger approximation.

4.2. Mass accretion rate

In the limit of $\xi_{\text{min}} \rightarrow 0$, the mass evolution rate due to mergers obtained by integrating Eq. (19) with respect to ξ becomes infinity. This indicates that the mass evolution is dominated by numerous minor mergers with small ξ , rather than rare major mergers. For an appropriate time interval, most of halos with similar masses would evolve with similar rates through minor mergers and the accretion, while a small fraction of halos experience abrupt growth due to major mergers. To express the continuous accretion, we adopt the median value of the total MAR in N-body simulations, in which the contribution of major mergers may be negligible.

The total MAR is defined as $\frac{dM}{dz} = -(M_0 - M_1)/\Delta z$, where M_0 is the descendant mass at z and M_1 is the mass of its most massive progenitor at $z + \Delta z$. The process of the mass increase, mergers or accretion, is not

specified here. According to [Fakhouri et al. \(2010\)](#), the median values of MAR in the two Millennium simulations is well fitted with the following formula;

$$\left\langle \frac{dM}{dz} \right\rangle_{\text{median}} = -3.58 \times 10^{12} M_{\odot} \left(\frac{h}{0.7} \right)^{-1} \times \left(\frac{M}{10^{12} M_{\odot}} \right)^{1.1} \left(\frac{1 + 1.65z}{1 + z} \right). \quad (21)$$

As discussed in [Fakhouri et al. \(2010\)](#), the mean MAR is overall larger than than median MAR, because the probability distribution of $\frac{dM}{dz}$ has a long tail in the high-accretion rate region. As the long tail, which boosts up the mean value, is mainly due to major mergers, the median value would be appropriate as the accretion rate in our definition.

4.3. Halo mass function

The merger tree calculation needs to reproduce the halo mass function (HMF), which describes the number of DM halos per unit comoving volume per unit mass. This can be written as,

$$\frac{dn}{d \ln M} = \frac{\rho_0}{M} f(\sigma, z) \left| \frac{d \ln \sigma}{d \ln M} \right|, \quad (22)$$

where ρ_0 is the mean mass density of the Universe, σ is the rms mass variance, and the function $f(\sigma, z)$ is called multiplicity function, whose functional form is determined analytically ([Press & Schechter 1974](#)) or empirically from the fit to the mass function in N-body simulations (e.g., [Sheth & Tormen 1999](#); [Jenkins et al. 2001](#); [Tinker et al. 2008](#); [Watson et al. 2013](#)).

The mass variance σ is calculated with a top-hat filter on a scale $R_M \equiv \left(\frac{3M}{4\pi\rho_0} \right)^{1/3}$ as

$$\sigma^2 = \int \frac{dk}{2\pi} k^2 P(k) |\hat{W}(kR_M)|^2, \quad (23)$$

where $P(k)$ is the linear matter power spectrum and $\hat{W}(\chi)$ is the Fourier transform of the top-hat window function, which is expressed as

$$\hat{W}(\chi) = \frac{3[\sin(\chi) - \chi \cos(\chi)]}{\chi^3}. \quad (24)$$

The radius R_M is larger than the physical radius of galaxy clusters R_{Δ} (Eq. (13)), since the mass density in clusters is generally larger than the mean mass density of the Universe.

The matter power spectrum, $P(k)$, in Eq (23) is conventionally expressed as

$$P(k) = A_8 k^{n_s} T^2(k), \quad (25)$$

where $T(k)$ is the transfer function, and n_s is the slope of the primordial power spectrum. The deformation from the primordial power spectrum at each scale is expressed by $T(k)$. The calculation of $T(k)$ includes technical challenges, because it is affected by, for example, various damping processes due to interaction between matters and relativistic particles. In this study, we adopt $T(k)$ generated with the public code CAMB.py ([Lewis et al. 2000](#)). The normalization A_8 is calculated from the cosmological parameter, σ_8 , which is the mass variance on a scale of $8h^{-1}$ Mpc. We adopt $n_s = 0.97$ and $\sigma_8 = 0.81$ from [Planck Collaboration et al. \(2020\)](#).

From Eq. (23), we can calculate the rightmost factor of Eq. (22);

$$\frac{d \ln \sigma}{d \ln M} = \frac{3}{2\sigma^2 \pi^2 R_M^4} \int_0^\infty \frac{d\hat{W}^2}{dM} \frac{P(k)}{k^2} dk. \quad (26)$$

Under the PS formalism, the multiplicity function, $f(\sigma, z)$, appearing in Eq (22) becomes universal to the changes in redshift and cosmological parameters and has an expression of $f_{\text{PS}}(\sigma) = \sqrt{\frac{2}{\pi}} \frac{\delta_c}{\sigma} \exp \left[-\frac{\delta_c^2}{2\sigma^2} \right]$, where $\delta_c = 1.69$ is the threshold parameter for the density fluctuation. However, we adopt the empirical formula for the multiplicity function given by [Tinker et al. \(2008\)](#), which agrees with the results in N-body simulations, as

$$f_{\text{T}}(\sigma, z) = A_{\text{T}} \left(\left(\frac{b}{\sigma} \right) + 1 \right) \exp \left[-\frac{c}{\sigma^2} \right], \quad (27)$$

with best-fit parameters, $A_{\text{T}} = 0.186(1+z)$, $a = 1.47(1+z)^{-0.06}$, $b = 0.3(1+z)^{-\zeta}$, $c = 1.19$, and $\zeta = \exp \left[-\left(\frac{0.75}{\Delta_{\text{vir}}/75} \right) \right]$, where Δ_{vir} is the overdensity with respect to ρ_0 within the sphere of radius R_M . We adopt $\Delta = 500$ to compare with the mass of the sample clusters in radio observations (Sect. 3).

4.4. Monte Carlo Simulation

For the initial state, we prepare $N = 4,000$ halos at $z = 0$ in the mass range of $[10^{13} M_{\odot}, 10^{16.5} M_{\odot}]$. To realize the mass distribution consistent with the HMF of [Tinker et al. \(2008\)](#), each halo is weighted with the HMF.

In our MC algorithm, the halo mass decreases through the mergers and the accretion as the time goes back to higher redshifts. The occurrence of a merger with each ξ in each time step is simulated with a random uniform number \mathcal{R} in the interval 0 to 1. When $\mathcal{R} < \mathcal{P}(M_0, \xi, z)$, the descendant halo with mass M_0 split into two progenitor halos with masses of $M_1 = M_0/(1 + \xi)$ and $M_2 = \xi M_0/(1 + \xi)$. This criterion is adopted for each ξ in each time step. When $\mathcal{R} \geq \mathcal{P}(M_0, \xi, z)$ for all ξ , the mass decreases only through the accretion.

In very rare cases, two or more mergers occur in one time step with different ξ . In this case, we choose M_1 as the mass of the most massive progenitor and M_2 as the sum of the rest, and redefine the mass ratio of the event as $\xi = M_2/M_1$. For example, in an event where a descendant halo with a mass of M_0 split into three haloes with $M_a > M_b > M_c$, we set $M_1 = M_a$ and $M_2 = M_b + M_c$. The ratio $\xi = M_2/M_1$ can be larger than unity in this case.

The boundary between the merger and accretion is ambiguous, so that the simple summation of $\Delta M = M_2 + \Delta M_{\text{median}}$, where $\Delta M_{\text{median}} = \langle dM/dz \rangle_{\text{median}} \times \Delta z$, would overestimate the mass evolution in each time step in our computation. Thus, we set $\Delta M = \Delta M_{\text{median}}$ for $M_2 < \Delta M_{\text{median}}$, considering that the contribution of frequent minor mergers are effectively included in ΔM_{median} . When $M_2 > \Delta M_{\text{median}}$, the halo mass at $z + \Delta z$ is chosen to be $M_1 = M_0 - M_2$ to account for the abrupt growth due to the major merger. Our code also follows the evolution of sub-progenitors with masses larger than $10^{13} h^{-1} M_\odot$, although those trees are not used in the following analysis. When multiple mergers occur in one time step, although such event hardly occurs, two or more sub-progenitors are produced in that step.

An example of the MC merger tree is shown in Figure 5 (left). Figure 5 (right) compares the HMF obtained from our MC merger tree with the fitting form of Tinker et al. (2008). Starting from the HMF given by Tinker et al. (2008) at $z = 0$ (blue), the HMF evolution shows a good agreement with the fitting formula at higher redshifts. Our method slightly (a factor of $\lesssim 2$) overproduce halos at a higher redshift ($z > 1.0$). However, since galaxy clusters above $M > 10^{14} M_\odot$ are mostly formed at a low redshift, that difference does not affect our discussion in the following sections. Although better match at higher redshifts would be achieved by tuning the parameters appearing in Eqs. (19) and (21), we adopt the same parametrization as Fakhouri et al. (2010) for simplicity.

5. STATISTICAL STUDY ON THE MERGER-RH CONNECTION

In this section, we study the connection between the halo merger and the occurrence of RHs, using the MC merger tree (Section 4). The RH survey observations have revealed that only a fraction of clusters host RHs, and they are preferentially found in merging systems (e.g., Buote 2001).

We assume two conditions for the RH onset: mass-ratio condition and break-frequency condition (Section 5.1). Based on the RH lifetime obtained in Sec-

tion 3, we model the mass dependence and time evolution of the radio power in Section 5.2. A cluster is categorized as a RH only when the radio power at the observation epoch is larger than the minimum value for the detection (Section 5.3). In Section 5.4, we discuss the constraints on model parameters by calculating the fraction of clusters with RHs, f_{RH} , and comparing it with the observation (Cuciti et al. 2021a).

The mass of clusters in those observations is defined with the over-density with respect to the cosmic critical density, while our MC merger tree refer to the mean mass density. We multiply a factor of $\Omega_m^{1/2}$ to convert the mass in merger tree into the observational mass (see also Enßlin & Röttgering 2002).

5.1. Criteria for the onset

We introduce two conditions for the onset of the radio emission in the ICM. The first one is called *mass-ratio condition*, which is a simplified approach using a threshold for the merger mass ratio, ξ_{RH} . This model is based on the idea that the merger event with larger ξ would dissipate a larger gravitational energy and thus would enhance the non-thermal emission more efficiently. We treat ξ_{RH} as a model parameter and do not consider its dependence on the total mass or redshift. We basically follow the procedure of Cassano et al. (2016) and discuss the observational constraints on ξ_{RH} . The number of merger events that satisfies $\xi > \xi_{\text{RH}}$ decreases with increasing ξ_{RH} . For a given lifetime of RHs (see Section 5.2 for detail), we can determine the value of ξ_{RH} that can explain the observed RH fraction f_{RH} .

We need to take into account the effect of the electron cooling. When the secondary injection is neglected, the reacceleration of CREs balances with the radiative cooling at a certain energy scale, which causes a spectral steepening at the break frequency ν_b . The second condition for the onset is called *break-frequency condition*, i.e., ν_b should be large enough to reproduce typical power and spectral index of RHs. Note that relatively steep spectral index around 1.4 GHz could be explained with $\nu_b < 1.4$ GHz (e.g., Cassano & Brunetti 2005).

For this requirement, we introduce another parameter that quantifies the efficiency of the reacceleration induced by a merger event. The parameter is η_t , the fraction of the turbulent energy to the merger kinetic energy. We use the formalization explained in Appendix B to calculate the reacceleration efficiency, or its timescale, t_{acc} , of each merger event as a function of η_t , M and ξ .

In this model, we firstly set ν_b around 1.4 GHz. The case with different ν_b will be discussed in Section 5.4.2. A merger can ignite the emission, whose spectral feature matches with the typical observed one, only when the

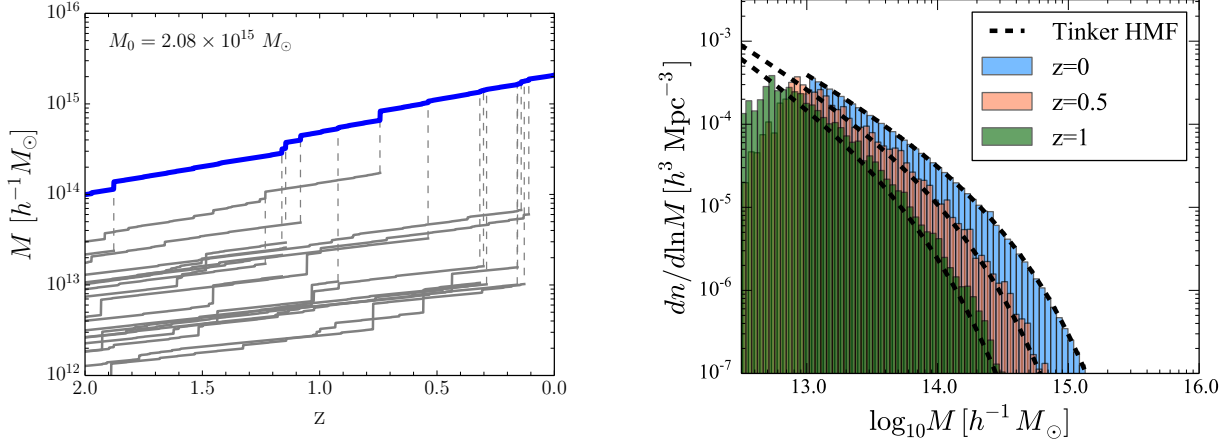


Figure 5. Left: An example of MC merger tree. The blue line shows the evolution of the most massive progenitor, while the gray lines correspond to the sub-progenitors. The merger between progenitors are expressed with the dashed lines. Right: HMFs constructed with the Monte Carlo merger trees (histogram) compared with the fitting function by Tinker et al. (2008) (dashed lines). The HMF at $z=0.0$ (blue), 1.0 (orange), 2.0 (green) are shown.

acceleration is efficient enough to balance or overcome the cooling at a given ν_b , i.e., $t_{\text{acc}} \leq t_{\text{cool}}|_{\nu=\nu_b}$. The cooling time scale due to synchrotron and IC radiation in the Thomson limit is approximated as (e.g., Rybicki & Lightman 1985; Brunetti & Jones 2014)

$$t_{\text{cool}} = \gamma_b m_e c^2 \left[\left(\frac{2}{3} \right)^2 \sigma_T (\gamma_b - 1)^2 (u_B + u_{\text{CMB}}) \right]^{-1},$$

$$\approx 360 \text{ Myr} \left[\left(\frac{\gamma_b}{10^4} \right) \left\{ \left(\frac{B}{3.2 \mu\text{G}} \right)^2 + (1+z)^4 \right\} \right]^{-1} \quad (28)$$

where σ_T is the Thomson cross section, $u_B = B^2/8\pi$ and $u_{\text{CMB}} = 0.262 \text{ eV/cm}^3 (T_{\text{CMB}}/2.73 \text{ K})^4 (1+z)^4$ are the energy densities of the magnetic field and the cosmic microwave background (CMB), respectively, and the Lorentz factor γ_b is related to ν_b as $\nu_b = \frac{3eB}{4\pi m_e c} \gamma_b^2$. For simplicity, we fix $B = 3.2 \mu\text{G}$ and t_{cool} is treated as a function of z and ν_b . The acceleration timescale becomes shorter with a larger η_t , which leads to a larger f_{RH} for a fixed ν_b .

The spectrum of CRPs is free from the break feature, except for the ultra-high energies ($E > 10^{19} \text{ eV}$), where the timescale of diffusive escape is comparable to the reacceleration timescale. In addition, the radio emission at 1.4 GHz is mostly powered by the injection from CRPs in the secondary scenario, as seen in Section 3.1. Thus, we adopt the *break-frequency condition* only for the primary scenario.

5.2. Power of the radio halo

One of the main objectives of this paper is to calculate the luminosity function of RHs (RHLF). Combining the HMF and the criteria proposed in Section 5.1,

one can obtain the mass function of RHs. Enßlin & Röttgering (2002) used the empirical relation between the radio power and the cluster mass to transform the HMF into the RHLF.

The important improvement in our method is to include the time evolution of the radio luminosity discussed in Section 3. The calculation in Section 3 was done only for the Coma-like RH, and the relation between cluster mass and radio luminosity has not been provided there. Our model includes many parameters, not only explicitly, t_{acc} , α_{turb} , L_p^{inj} , and t_R , but also implicitly, e.g., α_{inj} , (B_0, η_B) (Eq. (18)), (r_c, β) (Eq. (3)), and the duration of the injection phase. Thus, it is not straightforward to extrapolate the results for a Coma-like cluster to other clusters with different masses.

In this section, we assume a simple power-law relation between the maximum radio power at the end of the reacceleration period and M_{500} like the previous study in Enßlin & Röttgering (2002). In Section 7, however, we try to derive that relation by solving the FP equations, assuming a mass dependence of those parameters.

Summarizing above, the radio luminosity at 1.4 GHz is expressed as a function of both mass and time. We write it as $P_{1.4}(M_{500}, t_R)$, where t_R is the time interval between the RH onset and the observation. As long as the mass-ratio condition is satisfied, we do not consider the possible dependence on ξ for $P_{1.4}$, although this parameter could affect the efficiency of the reacceleration (Cassano & Brunetti 2005). The mass-ratio condition, $\xi > \xi_{\text{RH}}$, may ensure the efficient reacceleration up to the electron energy responsible for 1.4 GHz emission, and we assume that all such mergers achieve a similar luminosity with a similar timescale. This simplification may be justified, if the merger rate is a steep function

with respect to ξ and a large fraction of RHs arise from mergers with a value close to the lower limit ξ_{RH} .

Since both the mass and the luminosity evolve with time, it is important to distinguish $P_{1.4} - M_{500}$ relation at the onset from that at the observation. The timescale of mass increment can be evaluated from Eq. (21), and it is about 5 Gyr for $M_{500} \approx 10^{15} M_{\odot}$. If the RH lifetime is much shorter than this timescale, as in the primary scenario, the mass evolution after the onset is almost negligible. However, that can be not the case for the secondary scenario, since the emission can last for the cosmological timescale (≈ 10 Gyr). We adopt a power-law relation between the peak luminosity and the mass at the onset as $P_{1.4}(t_{\text{R}}^{\text{peak}}) \propto M_{500}^{\alpha_M}$, which could satisfy the observed $P_{1.4} - M_{500}$ relation, neglecting the mass evolution during the reacceleration phase (≈ 500 Myr).

As shown in Figure 6, we adopt the temporal evolution of RHs extrapolated from the modeling of the Coma-like RH. We have assumed in Section 3 that the Coma-like RH is in the midst of the reacceleration phase and the peak luminosity has not been achieved. The maximum duration of the reacceleration phase was assumed to be $t_{\text{R}}^{\text{peak}} \approx 500$ Myr, which is close to the timescale of the turbulent cascade at the ≈ 500 kpc scale (Section 7). The peak luminosity of the Coma-like RH becomes almost two orders of magnitude larger than the luminosity at the pre-acceleration state.

In the secondary scenario, such a high luminosity is sustained even in the cooling phase (Figure 3). We focus on the radio luminosity at 1.4 GHz and neglect the slight decline of the luminosity after the transition to the cooling phase. In the secondary scenario, we adopt a constant value of $P_{1.4}(M_{500}, t_{\text{R}})$ after the peak time, which is expressed as

$$\begin{aligned} \left(\frac{P_{1.4}(M_{500}, t_{\text{R}})}{10^{24.5} \text{ W/Hz}} \right) &= 10^{A_{\text{RH}}} \left(\frac{M_{500}}{10^{14.9} M_{\odot}} \right)^{\alpha_M} \\ &\times \left[\Theta(t_{\text{R}}^{\text{peak}} - t_{\text{R}}) 10^{2.0 \left(\frac{t_{\text{R}} - t_{\text{R}}^{\text{peak}}}{t_{\text{R}}^{\text{peak}}} \right)} \right. \\ &\left. + \Theta(t_{\text{R}} - t_{\text{R}}^{\text{peak}}) \right], \end{aligned} \quad (29)$$

where $\Theta(x)$ is the Heaviside step function, and $10^{A_{\text{RH}}} \left(\frac{M_{500}}{10^{14.9} M_{\odot}} \right)^{\alpha_M}$ corresponds to the peak luminosity for the descendant mass M_{500} . The overall normalization A_{RH} is considered to be a constant, and treated as a model parameter.

In the primary scenario, the RH would revert to the radio-quiet state within a few times the cooling timescale. We assume an exponential decay after the

peak time as

$$\begin{aligned} \left(\frac{P_{1.4}(M_{500}, t_{\text{R}}, z)}{10^{24.5} \text{ W/Hz}} \right) &= 10^{A_{\text{RH}}} \left(\frac{M_{500}}{10^{14.9} M_{\odot}} \right)^{\alpha_M} \\ &\times \left[\Theta(t_{\text{R}}^{\text{peak}} - t_{\text{R}}) 10^{2.0 \left(\frac{t_{\text{R}} - t_{\text{R}}^{\text{peak}}}{t_{\text{R}}^{\text{peak}}} \right)} \right. \\ &\left. + \Theta(t_{\text{R}} - t_{\text{R}}^{\text{peak}}) \exp \left[- \left(\frac{t_{\text{R}} - t_{\text{R}}^{\text{peak}}}{t_{\text{cool}}(z)} \right) \right] \right], \end{aligned} \quad (30)$$

where t_{cool} is the cooling timescale at 1.4 GHz. Since the Coulomb cooling is negligible at higher energies ($\gamma > 10^3$), t_{cool} is calculated from Eq. (28). We substitute the Lorentz factor corresponding to 1.4 GHz for γ_b . As in Section 5.1, we fix $B = 3.2 \mu\text{G}$ for the magnetic field. In this case, t_{cool} only depends on z .

The relation between the peak ($t_{\text{R}} = t_{\text{R}}^{\text{peak}}$) luminosity and the mass is shown in the left panel of Figure 6. As a reference, we adopted $(\alpha_M, A_{\text{RH}}) = (3.5, 0.4)$. Those values are constrained from the observed fraction of RHs, and their number counts per observed flux (see Section 5.4). The observed power of RHs and the upper limits listed in the extended sample of Cuciti et al. (2021a) are plotted with black points and green arrows, respectively. The black lines are the sensitivity limits for NVSS and ASKAP at $z = 0.2$ (Section 5.3). The luminosities of some RHs, such as Abell 545, Abell 1995, and Abell 2744 are close to the assumed peak luminosity for their mass, indicating that they are in the transition from the reacceleration phase to the cooling phase.

In the right panel of Figure 6, we plot the assumed evolution of Eqs. (29) and (30). We have adopted t_{cool} at $z = 0$ for the primary scenario.

As discussed in Section 3.2, the CR injection rate does not revert to that at the pre-reacceleration state, when a certain amount of CRPs are injected as primaries. However, we have neglected this effect in Eq. (30) in order to treat each merger event independently.

5.3. Observational limit

To estimate the RH number expected in the previous and future radio surveys, we need the minimum flux detectable in those surveys. Cassano et al. (2010) proposed two criteria for the detection: brightness-based criterion and flux-based criterion. In their brightness-based criterion, the mean flux within the halo radius θ_{H} is required to be larger than the rms noise F_{rms} by a factor of ζ_1 (see also Cassano et al. 2012),

$$\begin{aligned} f_{\text{min}} &= 1.4 \times 10^{-4} \text{ mJy } \zeta_1 \left(\frac{F_{\text{rms}}}{\mu\text{Jy}} \right) \\ &\times \left(\frac{\theta_b}{10 \text{ arcsec}} \right)^2 \left(\frac{\theta_{\text{H}}}{\text{arcsec}} \right)^2, \end{aligned} \quad (31)$$

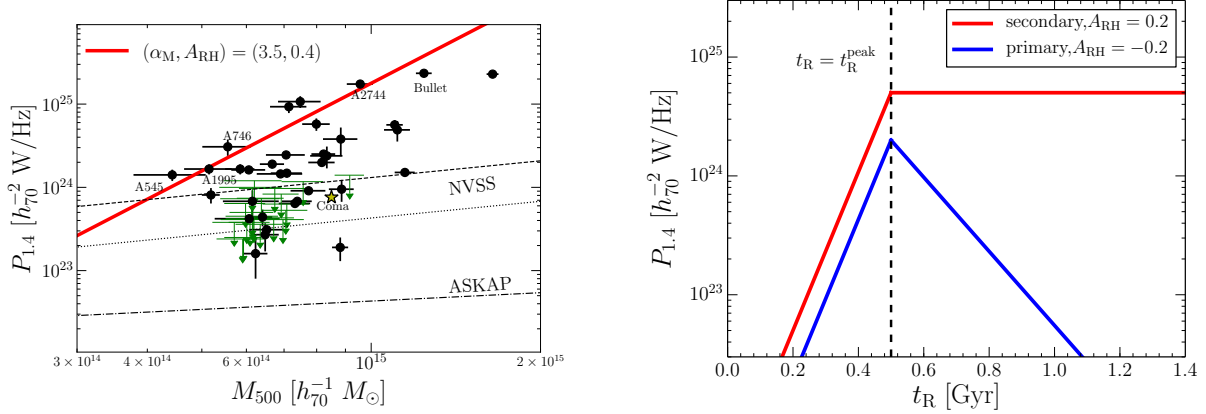


Figure 6. Mass and time dependence of the RH luminosity modeled in Section 5.4. Left: The red solid line shows the mass dependence of the peak luminosity. The black lines show the sensitivity limits for the NVSS (dashed: $R_H = 0.35R_{500}$, dotted: $R_H = 0.2R_{500}$) and the ASKAP (dot-dashed) survey. Data points are taken from Cuciti et al. (2021a). The Coma RH is shown with the yellow star. Right: The solid lines show the evolution model of the RH luminosity, which are expressed with Eqs. (29) and (30) for the secondary (red) and the primary (blue) scenarios, respectively. We assumed $M_{500} = 10^{14.9} M_{\odot}$ for both the lines, while different values for A_{RH} are adopted to improve the visibility. The vertical dashed line shows the peak time.

where θ_b is the angular size of the beam.

According to Cuciti et al. (2021a), the RHs typically have a volume of $(R_H/R_{500})^3 \approx 0.06 - 0.15$ except for a few of small RHs, such as the RHs in Abell 2218 and Abell 3411, for which $(R_H/R_{500})^3 \approx 0.01$. We adopt $\theta_H = 0.35\theta_{500}$ as the typical size of RHs, where θ_{500} is the angular size corresponding to R_{500} , which can be calculated for a given M_{500} with Eq. (13). For comparison, we will present the results also for $\theta_H = 0.2\theta_{500}$, which is the conventional threshold that distinguishes giant radio haloes from radio mini halos (e.g., Giacintucci et al. 2017).

The threshold for the flux depends on the mass and the redshift $f_{\min} = f_{\min}(M_{500}, z)$, as larger fluxes are required to detect larger mass RHs. The flux is evaluated at $\nu_{\text{obs}} = 1.4$ GHz, which is related to the emission power at 1.4 GHz as $f_{1.4} = (1+z)^{1-\alpha_{\text{syn}}} P_{1.4}/(4\pi D_L(z)^2)$, where α_{syn} is the spectral index of the RH (Section 1). Most RHs have α_{syn} in the range $-1.4 < \alpha_{\text{syn}} < -1.1$ (e.g., Giovannini et al. 2009). In the following, we fix $\alpha_{\text{syn}} = -1.2$ for all RHs in our merger tree.

The flux-based criterion of Cassano et al. (2012) is derived by assuming that the RH is detectable when the integrated flux within $0.5\theta_H$ gives a signal to noise ratio ζ_2 . In this case, f_{\min} can be written as

$$f_{\min} = 1.43 \times 10^{-3} \text{ mJy } \zeta_2 \left(\frac{F_{\text{rms}}}{10 \mu \text{ Jy}} \right) \times \left(\frac{10 \text{ arcsec}}{\theta_b} \right) \left(\frac{\theta_H}{\text{arcsec}} \right). \quad (32)$$

The dependence on the halo size θ_H is weaker than that in the brightness-based limit (Eq. (31)). Following Cassano et al. (2012), we adopt $\zeta_1 \approx 3$ and $\zeta_2 \approx 10$, as those

values give a number count consistent with the NVSS observation (Giovannini et al. 1999) in their calculation. The rms noise and the beam size for the NVSS survey are assumed to be $F_{\text{rms}} = 0.45$ mJy and $\theta_b = 45$ arcsec, respectively. We adopt them with Eq. (31) for the comparison with the NVSS data in this section, and use Eq. (32) with $(F_{\text{rms}}, \theta_b) = (10 \mu \text{ Jy}, 25 \text{ arcsec})$ to estimate the number count in the ASKAP survey in Section 9.

5.4. Occurrence of RHs

5.4.1. mass-ratio condition

First, we discuss the case where the onset is triggered by the condition $\xi > \xi_{RH}$. In this model, we have three model parameters: ξ_{RH} , α_M , and A_{RH} . The observed fraction of RHs and the luminosity function (Section 5.5) give constraints on those parameters. Cuciti et al. (2021a) reported that the fraction of RHs, f_{RH} , is ≈ 0.7 in the high-mass (HM) bin ($8.0 \times 10^{14} < M_{500} < 12.0 \times 10^{14}$), while it drops to ~ 0.35 in the low-mass (LM) bin ($5.7 \times 10^{14} < M_{500} < 8.0 \times 10^{14}$) in a sample of clusters from the *Planck* SZ catalogue. When the small halos and the ultra-steep spectrum radio halos (USS-RHs) (e.g., Brunetti et al. 2008) are excluded from the statistic, $f_{RH} \approx 0.33$ in the HM bin and $f_{RH} \approx 0.23$ in the LM bin.

We adopt a Monte Carlo procedure to calculate the fraction f_{RH} and its statistical error in our MC merger tree. We randomly extract a sub-sample of clusters from our merger tree, and calculate f_{RH} as a ratio between radio-loud and radio-quiet cluster. The size of the sub-sample is taken to be the same as the observation (Cuciti et al. 2021b), i.e., 60 clusters for the LM bin and 15

clusters for the HM bin. Those sub-samples are parts of the population with masses in the LM or HM bin at some time within the sampling range of redshift ($0.088 < z < 0.33$). If the radio flux of a halo, calculated with Eq. (29) or Eq. (30), is larger than the observational limit (Eq. (31)) at a given redshift, the halo is counted as a radio-loud one, while halos with a flux below the above criteria are regarded as radio-quiet one. The observation redshift ($0.08 < z < 0.33$) is divided into 50 bins, and we calculate the mean value of f_{RH} , weighting each redshift bin equally. The time interval t_{R} in Eq. (29) or (30) is measured from the most recent merger that satisfies the condition $\xi > \xi_{\text{RH}}$ before the observation.

The observed fraction could be reproduced in our merger tree by tuning the model parameters. Since the merger rate is larger for smaller ξ (Eq. (19)), one can expect more RHs for smaller ξ_{RH} . The parameter A_{RH} , which regulates the typical radio flux, also affects the RH fraction.

For any ξ_{RH} , we can find a parameter sets of $(\alpha_M, A_{\text{RH}})$ to reproduce the observed f_{RH} and its mass dependence. However, there should exit a typical mass for a given luminosity of RHs, considering the observed RHLF and the MF of clusters. For example, in the models with $A_{\text{RH}} \geq 1.0$ and $\alpha_M = 3.5$, even low-mass RHs with $M_{500} \leq 5 \times 10^{14} M_{\odot}$ can be observable with the NVSS sensitivity, and such a model overproduces the RH number count (Figure 9, Section 5.5). Thus, the parameter A_{RH} is constrained to be $A_{\text{RH}} \approx 0.5$.²

If the mass dependence of f_{min} is significantly weak, the assumed peak luminosity-mass relation naturally leads to the positive mass dependence of f_{RH} . However, the observed mass dependence is not significant to give a definite constraint on the parameters. We temporarily adopt α_M similar to the one adopted from the fitting to the observed RH, i.e. $\alpha_M = 2.5-4.0$. This ensures a reasonable fit to the observed number count (Section 5.5). In Section 7, we show that a similar mass dependence can be reproduced by calculating the peak luminosity for clusters with various masses. On the other hand, the threshold ξ_{RH} does not largely affect the mass dependence of f_{RH} , since the merger rate has a weak mass dependence.

We search for the best fit value of ξ_{RH} for given $(\alpha_M, A_{\text{RH}})$ in the range discussed above, and find $\xi_{\text{RH}} \approx 0.2$ and $\xi_{\text{RH}} \approx 0.01$ for the secondary and the primary models, respectively. The values of the three parameters, constrained from both the observed f_{RH} and the number count (Figure 9), are listed in Table 2. Here, we

Table 2. Model parameters compatible with the observed RH fraction

model	(i)	(ii)	(iii)	(iv)
scenario	secondary	primary	primary	primary
$(\alpha_M, A_{\text{RH}})$	(3.5, 0.4)	(3.5, 0.4)	(4.0, 0.2)	(4.0, 0.2)
ξ_{RH}	0.25	0.009	—	—
ν_{b}	—	—	1.4 GHz	500 MHz
η_{t}	—	—	0.65	0.5
$\langle f_{\text{RH}} \rangle^a$	0.38	0.32	0.21	0.22

NOTE—^a mean value of f_{RH} . The fraction for $R_{\text{H}} > 0.35 R_{500}$ in LM and HM bins are weighted with the sample size of each bin.

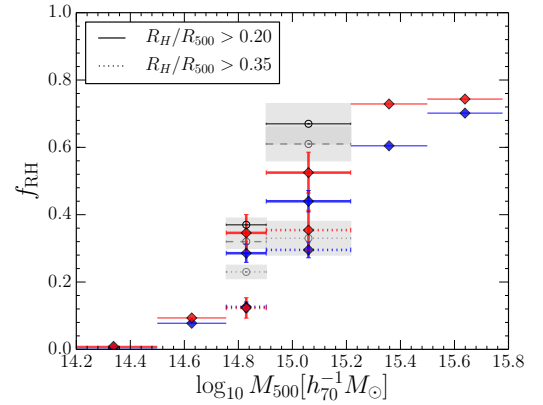


Figure 7. The fraction of RH clusters in six mass bins averaged within $0.088 < z < 0.33$ (red: secondary scenario, blue: primary scenario). The errors in the models (1σ) due to statistical fluctuation are given by $N = 100$ trials of the MC sampling. The gray lines show the observed fraction for three cases: small halos and USSRHs are counted as RHs (solid), USSRHs are considered as RHs but small haloes are considered as non-RHs (dashed), and both USSRHs and small halos are considered as non-RHs (dotted), adopted from Cuciti et al. (2021a). The shaded region show the 1σ error. See the text for further explanations.

refer the secondary and the primary models as model (i) and (ii), respectively. To study the impact of different ξ_{RH} and $P_{1.4}(M_{500}, t_{\text{R}})$ on the observable quantities, we adopt the same $(\alpha_M, A_{\text{RH}}) = (3.5, 0.4)$ for both the models. Possible constraints from the correlation between the RH occurrence and the X-ray morphological disturbance will be discussed in Section 6.

In Figure 7, we show f_{RH} for models (i) and (ii). The errors in the models due to statistical fluctuation are given by $N = 100$ trials of the MC sampling. The gray points and the shaded region show the observed fraction and its 1σ uncertainty associated with the statistical error on the masses, adopted from Cuciti et al. (2021a).

² A larger value of A_{RH} is preferable for a larger α_M .

The calculation was carried out for the two different thresholds for the halo size: $R_H > 0.2R_{500}$ and $R_H > 0.35R_{500}$. The contribution of the RHs with a small apparent size is excluded in the latter case. If small halos are excluded (points with dotted error bars), the fraction f_{RH} is about 10–30%, while it becomes 30–50% when small halos are included (points with solid error bars). The mean value of f_{RH} within LM and HM bins are shown in Table 2, where small halos are included. Both the models are in good agreement with the observed value, $\langle f_{RH} \rangle = 0.35 \pm 0.02$ (Cuciti et al. 2021a).

The difference in the best fit values for ξ_{RH} between the secondary and primary scenarios (models (i) and (ii)) is caused by the difference in the RH lifetimes. The longer lifetime in the secondary scenario requires less frequent onsets and thus a larger value for ξ_{RH} . In this scenario, RHs appear only after major mergers. This condition supports the expectation that only major mergers $\xi \approx 0.1$ can cause disturbances over the scale of giant RHs (Cassano et al. 2016). On the other hand, the short lifetime in the primary scenario requires a much smaller ξ_{RH} for the same (α_M, A_{RH}) . Thus, RHs need to be powered by frequent minor mergers.

Since the lifetime in model (i) is longer than the timescale of the mass evolution, a RH observed with a certain mass, M_{obs} , can have the low radio luminosity corresponding to a smaller mass, $M_{onset} < M_{obs}$. Since the relative margin between the peak luminosity and the observational limit is enough for larger masses (see Figure 6), more “aged” RHs (larger t_R), can contribute to the number count in higher mass bins. In other words, almost all of the RHs in lower mass bins are driven by recent ($t_R \lesssim 1$ Gyr) mergers, while the count in the higher mass bins can include RHs with larger t_R (> 1 Gyr). On the other hand, in model (ii), ages of RHs should be similar in all mass bin.

5.4.2. Break-frequency condition

In this section, we discuss the *break-frequency condition* in the primary model. In the models (iii) and (iv), we observe the competition between the acceleration and the cooling (Section 5.1). These models are basically compatible with model (ii) but described with different parameters, ν_b and η_t . As long as the same luminosity evolution is assumed, mergers with $\xi \gtrsim 0.01$ are required for the RH onset to explain the observed f_{RH} and number count.

We adopt a slightly steeper $P_{1.4} - M_{500}$ relation for models (iii) and (iv), as it provides a better fit to the mass dependence of f_{RH} for the primary scenario. Because we have not considered the redshift dependence in the parameters, while t_{cool} decreases with z (Eq (28)),

this model tends to predict a smaller f_{RH} at higher redshifts. That makes it difficult to fit simultaneously both the observed f_{RH} and the RH number count (Section 5.5), which is measured in lower redshifts. We find that the model is improved by the combination of a larger η_t and a smaller A_{RH} , rather than a smaller η_t and a large A_{RH} . Here, we adopt a slightly smaller A_{RH} compared to model (ii).

For $\nu_b = 1.4$ GHz, $\eta_t \approx 0.6$ is required. More than a half of the kinetic energy need to be dissipated into the compressible turbulence to achieve an efficient acceleration in mergers with $\xi \approx 0.01$. A smaller value of η_t can be allowed for a smaller ν_b (model (iv)). Even with those large η_t , models (iii) and (iv) predict a slightly small f_{RH} compared to the observed value, while the RH number count is well reproduced (Figure 9). A better model would be available with an even larger η_t (smaller A_{RH}). Therefore, if a large $\eta_t > 0.5$ or small ν_b is allowed, the observed RH statistics are reproduced even by minor mergers with $\xi \gtrsim 0.01$.

We again caution the limitation in our calculation; all RHs are assumed to follow the same luminosity evolution described with Eqs. (29) and (30), regardless of ξ . The apparent difficulty in the primary scenario, such as the requirement of a small value for ξ_{RH} or relatively large value for η_t , may be due to this simplification.

In addition, we have assumed that the magnetic field $B \approx 3.2 \mu\text{G}$ is fixed independently of M_{500} and z , while Cassano et al. (2006) assumed a positive mass dependence for B . For a smaller B , a slightly smaller η_t is applicable for the same ν_b .

5.5. Radio halo luminosity function

Figure 8 shows total RHLF calculated in our model at different redshifts by directly counting the RH number in our MC merger tree. Any observational limits are not included in this figure. Because we do not impose any conditions concerning the mass for the RH onset, a large number of RHs with low luminosities are predicted. Both the secondary and primary models predict similar redshift evolution. The RHLF at $z = 0$ is well approximated with that calculated from the HMF and the typical $P_{1.4} - M_{500}$ relation obtained from observations (e.g., Cassano et al. 2013), assuming mean occurrence of $f_{RH} = 0.3$ (dashed line) (see also Enßlin & Röttgering 2002). The best fit value of A_{RH} for the RHLF, $A_{RH} \approx 0.0 - 0.1$, becomes smaller than those assumed for reproducing the peak luminosity in Table 2, and it becomes similar to the fit to the observation (e.g., Cuciti et al. 2021a).

In Figure 9, we show the all-sky cumulative number counts of RHs observable with NVSS sensitivity

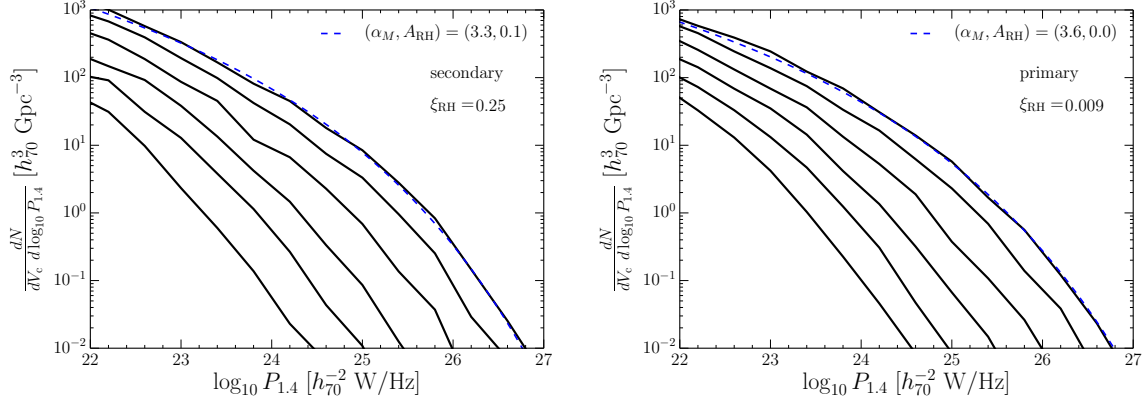


Figure 8. RHLF at different redshifts ($0 \leq z \leq 1.0$). From top to bottom, results for $z = 0.0, 0.2, 0.4, 0.6, 0.8$, and 1.0 are shown. Dashed lines are calculated with the HMF and the power-law scaling between $P_{1.4}$ and M_{500} , assuming the mean occurrence of $f_{\text{RH}} = 0.3$.

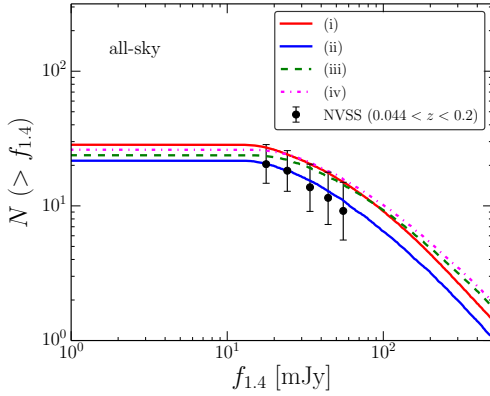


Figure 9. Cumulative number count of RHs observable with NVSS sensitivity for the different models listed in Table 2. The black points show the NVSS number count within $0.04 < z < 0.2$ for the all-sky, adopted from Cassano et al. (2012).

and compare them with the number count in the NVSS follow-up (Giovannini et al. 1999) of the XBACs sample (Ebeling et al. 1996). In this figure, we take into account not only the observational limit explained in Section 5.3 but also the X-ray flux limit in the XBACs sample ($f_X > 5.0 \times 10^{12}$ [erg/cm²/s]), where we have used the scaling relation reported in Yuan et al. (2015) to translate the radio power at 1.4 GHz $P_{1.4}$ into the cluster X-ray luminosity L_X . The size of RH is assumed to be $R_H > 0.35 R_{500}$, excluding the small RHs. The parameters listed in Table 2 agree with the observed count (data points are adopted from Cassano et al. (2012)), ensuring the compatibility between the observations and our models. In Section 9, we discuss the number count in future high-sensitivity survey.

6. CORRELATION WITH MERGING SYSTEMS

RHs are preferentially found in clusters showing the signatures of merger activities (e.g., Schuecker et al. 2001; Govoni et al. 2004). In this section, we quantify the fraction of RHs classified as a merging cluster in observations using our merger tree. We employ the same method used for the calculation of f_{RH} with the *mass-ratio condition* (Section 5.4.1).

The RH lifetime in our secondary scenario is comparable to the loss timescale of CRPs, so it can exceed the dynamical timescale of cluster mergers. Thus, the secondary scenario predicts a fraction of RHs hosted in relaxed clusters. This scenario should be tested in the light of the observed correlation between the occurrence of RHs and the dynamical disturbance in X-ray morphology.

According to Cassano et al. (2013), the fraction of all merging clusters, including both RHs and non-RHs, is about 60% in both LM and HM bins. Firstly, we try to recover this fraction in our merger tree, using a similar method to that in Section 5 (see also Cassano et al. 2016). We newly introduce two parameters, ξ_{mer} and t_{relax} . The former one, ξ_{mer} , is the threshold mass ratio, above which such a merger makes a descendant cluster disturbed enough to be classified as a merging system in the X-ray morphological analysis. The parameter t_{relax} is the timescale required for a merger system to recover a relaxed state, or the “lifetime” of the merging system.

We do not model the detailed merger dynamics with parameters to diagnose if clusters are merging systems, such as the concentration parameter, c , the centroid shift, w , and the power ratio, P_3/P_0 (e.g., Mohr et al. 1993; Buote 2001; Santos et al. 2008). Those parameters generally depend on various factors other than the mass ratio, e.g., the projection effect and the impact parameter of the merger.

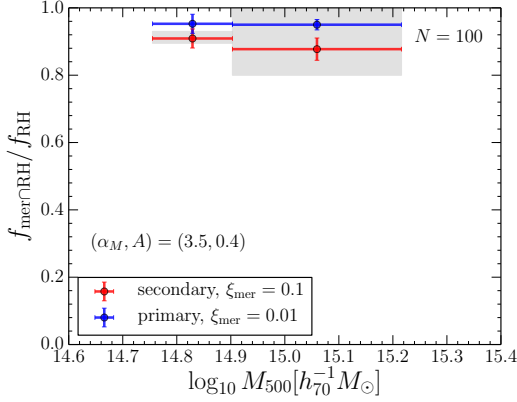


Figure 10. The conditional fraction of RHs in merging systems over the total fraction of RHs. The shaded region indicates the observed fraction in the sample of Cuciti et al. (2021a). The halo size is assumed to satisfy $R_H > 0.35R_{500}$.

Unlike Section 5, we fix ξ_{mer} and find t_{relax} that can explain the merging fraction of $\approx 60\%$, because the latter is less constrained from observations. As a reference value, we assume $\xi_{\text{mer}} = 0.1$ for the secondary scenario, which is close to the minimum mass ratio of observed RH-hosting clusters (Cassano et al. 2016). As in Section 5.4, we extract sub-sample of halos, which have masses in LM or HM bin within $0.088 < z < 0.33$. The redshift range is divided into 50 bins as before. A cluster is identified as a merging cluster only when the time interval between the merger and the observation is smaller than t_{relax} , i.e., $t_R \leq t_{\text{relax}}$. Under the above condition, we find that $t_{\text{relax}} = 3.6$ Gyr successfully explain the merging fraction of $\approx 60\%$ (see also Cassano et al. 2016).

In the next step, we calculate the fraction of RHs found in merging clusters over all RHs, $f_{\text{mer} \cap \text{RH}}/f_{\text{RH}}$, to test the correlation between the merging state and RHs. In the sample of Cuciti et al. (2021b), this fraction is 90%-100%. We use the same procedure as before to calculate that fraction in our merger tree; $f_{\text{mer} \cap \text{RH}}$ is defined as the fraction of clusters that show the radio power larger than the observational limit and also satisfy $t_R < t_{\text{relax}}$ at the observed epoch.

Figure 10 shows the results for models (i) and (ii). Excluding small RHs with $R_H \leq 0.35R_{500}$, we find that the fraction is compatible with the observation. Thus, most of RHs in our merger tree should show disturbed morphology at the observed epoch and are classified as merging systems. In other words, the time interval between the onset and the observation, t_R (Eq. (29)), is typically shorter than t_{relax} .

A similar discussion can be applicable for the primary scenario as well. Interestingly, as a small value for ξ_{RH} is required for this scenario, ξ_{mer} should also be small to

explain the tight correlation between RHs and merger systems. If $\xi_{\text{RH}} \ll \xi_{\text{mer}}$, there exists a large number of merger events whose mass ratios are large enough to generate RHs ($\xi_{\text{RH}} < \xi$), but too small to make an observable disturbance ($\xi < \xi_{\text{mer}}$). Such condition predicts that large fraction of RHs are in relaxed systems, which is clearly in tension with the observation. As a consequence, ξ_{mer} should be similar or smaller than $\xi_{\text{RH}} \approx 0.01$.

We adopt $\xi_{\text{mer}} = 0.01$ for the primary scenario and find that $t_{\text{relax}} = 1.1$ Gyr leads to the merger fraction of 60%. With those ξ_{mer} and t_{relax} , $f_{\text{mer} \cap \text{RH}}/f_{\text{RH}} \gtrsim 0.9$ is well reproduced in this scenario (Figure 10). However, that requirement for $\xi_{\text{mer}} \simeq 0.01$ seems problematic, since the mass ratio estimated from optical or near infra-red observations is typically $\xi \gtrsim 0.1$ for known merging clusters (Cassano et al. 2016).

The above difficulty in the primary scenario may be due to our simplified treatment of the turbulent energy. Since each merger event is treated independently, we have not considered the summation of the turbulent energy induced by continuous mergers. If this intermittent energy injection is considered, both ξ_{RH} and ξ_{mer} may be larger and the apparent difficulty in the primary scenario may be relaxed (see also Cassano & Brunetti 2005).

7. PEAK LUMINOSITY-MASS RELATION

In Section 5.2, we have introduced a simple power-law relation between the peak luminosity and the mass of RHs. In this section, we verify if such a steep relation could arise from the mass dependence of the reacceleration efficiency. We extend the model used in Section 2 to RHs with various masses, assuming a mass scaling in the model parameter τ_{acc} .

In this section, we use a representative value for the acceleration timescale, τ_{acc} , which is the volume average of $t_{\text{acc}}(r) = p^2/(4D_{pp}(r))$ within $r < 0.5R_{500}$, where most of the radio emission is produced.

As seen in Nishiwaki et al. (2021), our turbulent reacceleration model is more sensitive to t_R or τ_{acc} than the duration of the injection phase, and the energy injection from the reacceleration is at least an order of magnitude larger than that from the injection. The steep mass-dependence of the peak luminosity could be due to the steep dependence on the ratio t_R/τ_{acc} .

7.1. Luminosity evolution in the reacceleration phase

First, we show the exponential increase of the radio luminosity in the reacceleration phase. We examine the Coma-like case as an example. We use the same model adopted in Section 2.5 with the same model parameters. The typical reacceleration timescale becomes

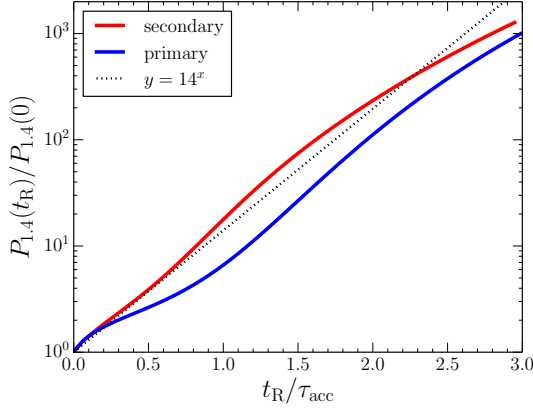


Figure 11. Time evolution of $P_{1.4}$ in the reacceleration phase. We adopt the same Coma-like model (Section 2.5), and the radio power is shown as a function of the duration of the reacceleration phase, t_R . The duration is normalized with the acceleration timescale of $\tau_{\text{acc}} = 253$ Myr and 231 Myr for the secondary and the primary models, respectively. Those are the mean value within $r < 0.5R_{500}$ for the Coma-like RH.

$\tau_{\text{acc}} = 253$ Myr and 231 Myr for the secondary and the primary scenarios, respectively.

In Appendix B, we roughly estimate the timescales, τ_{acc} and t_R^{peak} with the simple binary merger approximation. There, we introduce a parameter η_t , which quantifies the fraction of the turbulent energy to the merger kinetic energy. A merger is parameterized with the mass ratio ξ and the mass M_{500} . We find that the reacceleration with $\tau_{\text{acc}} \approx 250$ Myr could be induced by a merger with $\xi \approx 0.1$ and $M_{500} \approx 10^{15} M_\odot$ when $\eta_t \approx 0.15$. The duration of $t_R^{\text{peak}} \approx 500$ Myr assumed in Section 3 might correspond to the turbulent decay time at the injection scale but multiplied by a factor of ≈ 2 .

In Figure 11, we show the time evolution of $P_{1.4}$ during the reacceleration phase. The luminosity is normalized with the value at the beginning of the reacceleration phase, while t_R is normalized with τ_{acc} . The exponential increase of the luminosity can be seen in both the scenarios. The evolution in the secondary scenario can be approximated as $P_{1.4} \propto 14^x$, where $x = t_R/\tau_{\text{acc}}$.

As discussed in Section 3, the synchrotron at high frequencies is mostly powered by the enhanced injection from reaccelerated CRPs. That discussion seems in line with the evolution seen in Figure 11, as explained in the following. Since CRPs do not suffer from significant coolings, the hard-sphere type reacceleration causes the advection of the spectrum in the momentum space. At $t_R = \tau_{\text{acc}}$, the spectrum shifts to a higher energy by a factor of $e \approx 2.718$. As we have assumed $\alpha_{\text{inj}} = 2.45$ for the typical injection index, the production rate of secondary CREs, which is proportional to N_p , is increased

by $e^{2.45} \approx 11.59$, slightly lower than 14. The slight deviation from this estimate would come from the spectral evolution of CREs or the definition of the typical acceleration timescale τ_{acc} (Note that D_{pp} depends on the radius).

The luminosity evolution in the primary scenario (blue line in Figure 11) shows more complex features. The overall trend is slightly shallower than the secondary scenario, possibly because of the radiative cooling. It is characterised by the steepening around $t_R/\tau_{\text{acc}} \approx 1$ and subsequent flattening around $2t_R/\tau_{\text{acc}}$. Those features should be related to the spectral evolution of CREs. As seen in Nishiwaki et al. (2021), the CRE spectrum has a bump like-shape caused by the Coulomb cooling and the radiative cooling. The reacceleration shifts that bump towards higher energies.

7.2. peak luminosity for various masses

We calculate the peak luminosity of RHs with various masses, extending the model in Section 3, which was adopted for the Coma RH (Section 2.5). For this purpose, we introduce a scaling between the reacceleration parameter and the mass. As shown in Appendix B, under the simple binary merger approximation with zero impact parameter and the IK scaling for the compressible turbulence, one can find $\tau_{\text{acc}} \propto M_{500}^{-1/3}$. Thus, the reacceleration could be more efficient for larger masses. On the other hand, we assume that t_R^{peak} is independent of the mass for simplicity. This may be justified if the duration is regulated by the turbulent cascade timescale rather than the dynamical timescale of the merger (see Appendix B). The values of τ_{acc} and t_R^{peak} will be normalized at the Coma mass, $M_{500} \approx 8.5 \times 10^{14} M_\odot$.

We neglect the ξ dependence of the acceleration efficiency and the duration, although the acceleration efficiency is more sensitive to ξ than M_{500} (Figure 17 in Appendix B). In other words, all RHs are assumed to be generated through the mergers with the threshold value $\xi \simeq \xi_{\text{RH}}$, regardless of the mass. As noted in Section 5.2, the steep ξ dependence of the accretion rate ensures that events with $\xi \gg \xi_{\text{RH}}$ are negligible. More precisely, the ξ dependence would cause a scatter in the peak luminosity-mass relation. The parameters we adopt here can be interpreted as the merger-rate weighted means for $\xi_{\text{RH}} < \xi < 1$.

In addition to the above assumptions, we introduce following assumptions to make our model applicable to RHs with various masses:

- We adopt the beta-model of the ICM profile, where the core radius is scaled with the virial radius, $r_c \approx 0.2R_{500}$, and $\beta = 0.75$ is taken to be constant. Under the assumption of a constant baryon

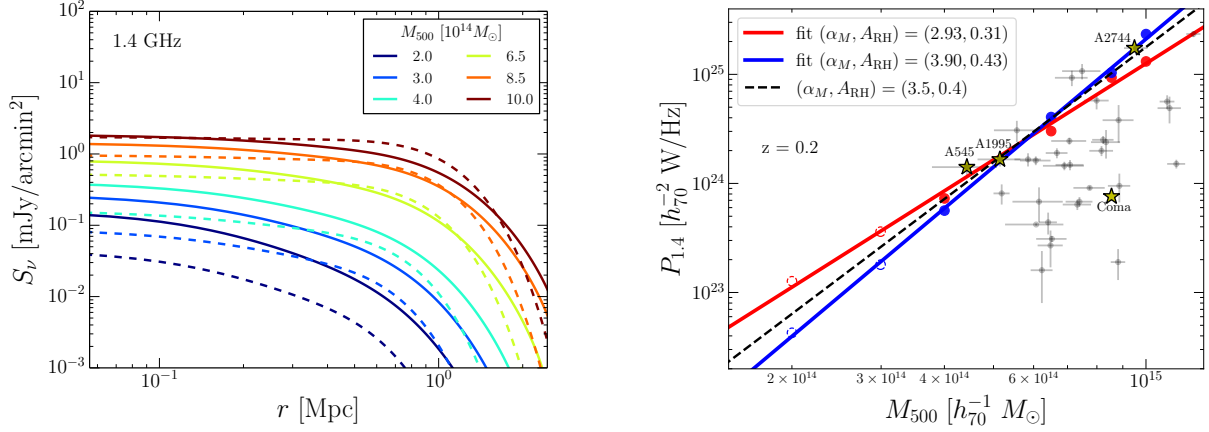


Figure 12. 1.4 GHz brightness profile for various masses at the peak time (left) and the mass dependence of the peak luminosity (right) in our model calculations. In the left panel, we show RH profiles with masses of $M_{500} = 2.0, 3.0, 4.0, 5.0, 6.5, 8.5, 10.0 \times 10^{14} M_\odot$. The results for different masses are distinguished by colors. The secondary and the primary scenarios are shown with solid and dashed lines, respectively. In the right panel, the red and blue circles show the calculated peak luminosity for the secondary and the primary scenarios, respectively. The clusters represented with open circles have masses smaller than the minimum mass in Cuciti et al. (2021a). We also plot the observed luminosities with thin black data points. Some of the RHs are highlighted with star symbols. We adopt $t_R^{\text{peak}} = 620$ Myr and 675 Myr for the secondary and the primary scenarios, respectively. The solid lines show the fits to the red and blue points, while the dashed line is the relation assumed in Section 5.4.

fraction for all masses (see, e.g., Allen et al. 2008, for the observational constraints), this leads to a constant central density of $n_0 \approx 3 \times 10^{-3} \text{ cm}^{-3}$.

- We adopt the same Eq. (18), B_0 , and η_B for the profile of the magnetic field, without any dependence on mass or redshift.
- We adopt Eq. (6) with $\beta = 0.75$ and $r_c \approx 0.2R_{500}$, and $\alpha_{\text{inj}} = 2.45$ for the primary CR injection. The volumetric CR injection rate at the center ($r = 0$) is scaled with the thermal energy density normalized by the model for the Coma cluster.
- We adopt the same index for the turbulent profile, α_{turb} , as Coma.
- The ICM temperature follows the observed mass-temperature relation (Vikhlinin et al. 2006):

$$\left(\frac{T}{5 \text{ keV}} \right) = \left(\frac{E(z)M}{M_5} \right)^{k_T}, \quad (33)$$

where $E(z) = H(z)/H_0$, $M_5 = 3.3 \times 10^{14} h^{-1} M_\odot$ and $k_T = 1/1.47 \approx 0.68$.

- All clusters are observed at redshift $z = 0.2$, which roughly corresponds to the mean redshift of the sample of Cuciti et al. (2021a).
- The duration of the injection phase is taken to be the time gap between $z = 0.2$ and the epoch when the cluster mass was a half of that at the observation calculated with Eq. (21).

The observations indicate that $\sim \mu\text{G}$ magnetic field is ubiquitous in nearby merging clusters, while some cool-core clusters could have a central field of a few $\sim 10 \mu\text{G}$ (e.g., van Weeren et al. 2019, for review). Recent low-frequency RH observation suggests that some distant clusters have similar magnetic field to those in nearby clusters (Di Gennaro et al. 2021).

With those assumptions, we calculate the peak luminosity of RHs with $M_{500} = 2, 3, 4, 5, 6.5, 8.5, 10.0 \times 10^{14} M_\odot$ at $z = 0.2$. The acceleration timescale averaged within $r < 0.5R_{500}$, τ_{acc} , is normalized at the Coma mass ($M_{500} = 8.5 \times 10^{14} M_\odot$) as $\tau_{\text{acc}} = 253$ Myr and 231 Myr for the secondary and the primary scenarios, respectively. With the scaling of $\tau_{\text{acc}} \propto M_{500}^{-1/3}$, τ_{acc} spans $237 \text{ Myr} < \tau_{\text{acc}} < 405 \text{ Myr}$ for the above mass range in the case of the secondary scenario. We use the value of peak luminosity assumed in Section 5.4 to derive the duration required to achieve the peak luminosity, t_R^{peak} . Adopting $(\alpha_M, A_{\text{RH}}) = (3.5, 0.4)$, the peak luminosity becomes $P_{1.4} = 1 \times 10^{24} \text{ W/Hz}$ at the Coma mass. We find that $t_R^{\text{peak}} = 620$ Myr and $t_R^{\text{peak}} = 675$ Myr can reproduce that luminosity at the Coma mass for the secondary and the primary scenarios, respectively. As noted before, t_R^{peak} is assumed to be constant with mass. With those assumptions, the peak luminosity increases with mass.

In the secondary scenario, the typical value of the average CR energy density in the RH volume ($r \leq 0.5R_{500}$), ϵ_{CR} , becomes $\approx 5\%$ of the thermal energy density at the peak state. As discussed in Appendix B, the acceleration timescale could be reproduced with

$\eta_t \approx 0.15$, $\xi \approx 0.2$ and $M_{500} \approx 10^{15} M_\odot$. With those values, the energy density of the compressible turbulence induced by a merger becomes $\approx 40\%$ of the thermal one. Thus, $\eta_{\text{CR}} \approx 12.5\%$ of the turbulent energy should be consumed for the CR acceleration.

In the primary scenario ($f_{\text{ep}} = 0.01$), we find $\epsilon_{\text{CR}} \approx 0.003\epsilon_{\text{th}}$ at the peak time. The energy density ϵ_{CR} is still dominated by CRPs even after the reacceleration. With the same values of η_t , ξ , and M_{500} as those in the secondary scenario above, only $\eta_{\text{CR}} \approx 0.75\%$ of the turbulent energy should be converted into the CR energy.

As seen in Section 5, however, $\xi_{\text{RH}} \approx 0.01$ rather than 0.2 is required to explain the observed fraction of RHs in the primary scenario. When ξ is taken to be 0.01 as the typical value, the turbulent energy fraction is estimated as $\approx 10\%$ of the thermal energy, then $\eta_{\text{CR}} \approx 3\%$ is required. On the other hand, a higher efficiency of the turbulent excitation ($\eta_t \approx 0.4$) is required for this scenario (Appendix B).

In the above discussion, the energy injection in the form of primary CR injection is not taken into account, since that is negligible compared to the energy injection by the reacceleration (Nishiwaki et al. 2021).

In the left panel of Figure 12, we show the brightness profiles at the peak time. Since a larger $t_{\text{R}}^{\text{peak}}/\tau_{\text{acc}}$ is assumed for higher masses, the overall brightness increases with mass. Note that all of those RHs are assumed to be at the same redshift, $z = 0.2$. The typical size, or the cut-off radius of the profile, also increases with mass. We have assumed that the core radius of the ICM (r_c) scales with R_{500} . The profile of the magnetic field, the CR injection, the turbulence for the reacceleration, and thus the synchrotron brightness also scale with R_{500} . The profiles in the primary scenario (dashed lines) are slightly flatter than the secondary scenario (solid lines), because of the flatter turbulent profile assumed in the primary scenario. In addition, the brightness in the primary scenario more steeply depends on the mass than the secondary scenario.

In the right panel of Figure 12, the red and blue points show the peak luminosity at 1.4GHz for the secondary and the primary scenarios, respectively. Those points are fitted with a power-law function $\left(\frac{P_{1.4}}{10^{24.5} \text{ W/Hz}}\right) = 10^{A_{\text{RH}}} \left(\frac{M_{500}}{10^{14.9} M_\odot}\right)^{\alpha_M}$. When the clusters with $M_{500} < 4 \times 10^{14} M_\odot$ are excluded (only filled points), the best fit values are $(\alpha_M, A_{\text{RH}}) = (3.24 \pm 0.18, 0.31 \pm 0.03)$ (secondary) and $(3.99 \pm 0.15, 0.44 \pm 0.02)$ (primary). We can reproduce the steep relation with $\alpha_M \approx 3 - 4$ for both the scenarios. The slope of the relation reflects the steepness of the luminosity evolution around $t_{\text{R}}/\tau_{\text{acc}} \approx 2$, shown in Figure 11. Since the dependence on $t_{\text{R}}/\tau_{\text{acc}}$

is larger in the primary scenario, the fit result in Figure 12 is also steeper than that in the secondary scenario. When the open circles, whose masses are smaller than the minimum mass of the sample of Cuciti et al. (2021b), are included in the fit, the slope becomes slightly shallower; $\alpha_M = 2.93$ and 3.90 for the secondary and the primary scenarios, respectively (solid lines).

8. GAMMA-RAY LIMITS IN THE SECONDARY SCENARIO

Since the long-living radio emission in the secondary scenario is sustained by the injection from re-accelerated CRPs (Section 3), gamma-ray emission is inevitable in this model. On the other hand, the observational efforts taken in the last decade have failed to detect diffuse cluster-scale gamma-ray emission, except for the possible detection from Coma (e.g., Xi et al. 2018; Abdollahi et al. 2020). The gamma-ray limits with *Fermi*-LAT constrain the CR-to-thermal pressure ratio to be smaller than $\approx 5\%$ (Ackermann et al. 2014). In this section, we discuss the compatibility between our secondary scenario and the *Fermi*-LAT observations for two RH-hosting clusters: Coma and A2744.

8.1. Coma cluster

In this section, we review the constraints on the hadronic model of the Coma RH. As discussed in Nishiwaki et al. (2021) and Section 2.5, the gamma-ray limit is not deep enough to exclude the model where all CREs are produced as secondaries ($f_{\text{ep}} = 0$), as long as the RH is in the midst of the reacceleration phase.

The Coma cluster is characterised by its low redshift $z = 0.0231$, and a deep limit on the gamma-ray flux is given by *Fermi*-LAT (e.g., Ackermann et al. 2016). The radio power $P_{1.4} \approx 7.6 \times 10^{23} \text{ [W/Hz]}$ is relatively low compared to other RHs with a similar mass (e.g., Cassano et al. 2013). The detailed RM measurement constrained the magnetic field (Bonafede et al. 2010), and the best fit value of its strength at the central region is $B_0 = 4.7 \mu\text{G}$.

Brunetti et al. (2017) show that the relatively deep gamma-ray limit given by Ackermann et al. (2016) requires a magnetic field several times stronger than that from RM measurement in the pure-hadronic scenario where the reacceleration of seed CREs and primary CREs are not considered, but this tension is relaxed when the reacceleration of CREs is taken into account. As confirmed in Nishiwaki et al. (2021), the ratio between synchrotron flux around 300 MHz and gamma-ray flux around 1 GeV, $F_{\text{radio}}/F_\gamma$, increases as the reacceleration proceeds. In Section 3, we have shown that the radio emission is energized by both the reacceleration of

the seed CREs and the fresh CRE injection from reaccelerated CRPs, and that the former component decays in the cooling phase. At a significantly later phase after the end of the reacceleration, the ratio $F_{\text{radio}}/F_{\gamma}$ eventually approaches the value expected in the pure-hadronic model.

We conclude that the RH is in the stage where the reacceleration of seed CREs is efficient, and not in the injection phase or the late stage of the cooling phase. As long as the Coma RH is assumed to be in the midst of the reacceleration phase or in the very early stage of the cooling phase, our model is not in strong tension with the gamma-ray limit under the magnetic field constrained from RM.

Recently, several papers on the analysis on Fermi data reported the detection of diffuse gamma-ray emission in the direction of Coma (Xi et al. 2018; Abdollahi et al. 2020; Adam et al. 2021). Although that emission is controversial because of the point source contamination, it is worth noting that the flux deduced from those analyses is comparable to the expectation in our secondary model (Nishiwaki et al. 2021).

8.2. Abell 2744

The galaxy cluster Abell 2744 is a merging cluster located at redshift $z = 0.307$. It hosts one of the most luminous RHs with power of $P_{1.4} = 1.74 \times 10^{25}$ [W/Hz] (e.g., Govoni et al. 2001). Compared to Coma, it has a similar mass of $M_{500} \approx 9.56 \times 10^{14} M_{\odot}$, but its radio luminosity is 23 times more luminous.

In section 5, we have shown that the observed $P_{1.4} - M_{500}$ relation can be reproduced by assuming the simple relation between the peak luminosity and the mass at the onset combined with the luminosity evolution studied in Section 3. As seen in the left panel of Figure 6, the radio power of A2744 almost corresponds to the peak value for its mass assumed in Section 5.2. This indicates that the RH is now close to the transition from the reacceleration phase to the cooling phase.

The recent radio observation has shown that the spectrum of the entire halo is well fitted with a single-power law with $\alpha_{\text{syn}} = -1.14$ between 150 MHz and 3 GHz, while the subregions of the RH show a spectral steepening towards higher frequencies (Rajpurohit et al. 2021). The SZ-decrement at 3 GHz is taken into account in that analysis.

We model the emission from A2744 using the assumptions explained in Section 7. One important difference from the model in the previous section is the spectral index; we here adopt a shallower one, $\alpha_{\text{inj}} = 2.2$, to fit the radio spectrum. As assumed in Section 7, the acceleration efficiency is scaled with the mass as $\tau_{\text{acc}} \propto M^{-1/3}$

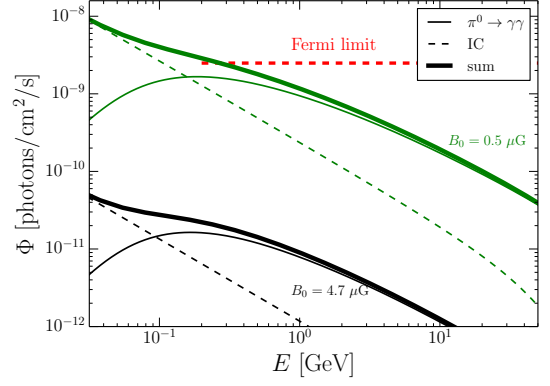


Figure 13. Expected gamma-ray flux from A2744 and the observational upper-limit for 0.2-100 GeV, adopted from Ackermann et al. (2010). The thin solid and the thin dashed lines show the $\pi^0 \rightarrow \gamma\gamma$ flux and the IC flux, respectively, while the thick lines show the total flux. In the case of $B_0 = 0.5 \mu\text{G}$ (green lines), we adopt a about 50 times larger CR injection rate to reproduce the radio emission.

and it becomes $\tau_{\text{acc}}(r_c) = 319$ Myr for the A2744 mass. Since the A2744 RH is at the very end of the reacceleration phase, we adopt the peak time obtained in the previous section, $t_{\text{R}}^{\text{peak}} = 620$ Myr for the observed state $t_{\text{R}} = t_{\text{R}}^{\text{peak}}$. Other model parameters, the turbulent profile and the volumetric CR injection rate, are the same as those for the Coma-like cluster. For the ICM profile, we adopt the beta-model but with the parameters given by Ota & Mitsuda (2004), i.e., $r_c = 600$ kpc and $\beta = 0.96$ (see also Ibaraki et al. 2014). The ICM temperature is scaled from Coma with the T-M relation (Eq. (33)). We adopt the same magnetic field profile as Coma (Eq. (18)), where we adopt same r_c as the ICM beta-profile. Our results for the spectrum and the spatial profile well agree with the radio observation as shown in Appendix C.

Based on this model, we compare the expected gamma-ray flux and the observational limit in Ackermann et al. (2010) (see Figure 13). The calculation method of gamma-ray emission due to π^0 decay and ICS is the same as that in Nishiwaki et al. (2021). The softening of the IC component above 10 GeV is artificial (due to maximum energy of CREs, see Section 2.1). With $(B_0, \eta_B) = (4.7 \mu\text{G}, 0.5)$, the expected gamma-ray flux becomes nearly two orders of magnitude lower than the Fermi limit. This gamma-ray limit rather constraints the minimum strength of the magnetic field (Jeltema & Profumo 2011). Adopting the same scaling of Eq. (18) with $\eta_B = 0.5$, we obtain $B_0^{\text{min}} \approx 0.5 \mu\text{G}$ for the minimum value for the central magnetic field (Figure 13), which is compatible with the previous study (Jeltema & Profumo 2011). In that case, the volumetric

CR injection rate should be larger by a factor of ≈ 50 to reproduce the observed radio flux. We can conclude that the current gamma-ray limit cannot exclude the hadronic origin of the radio-emitting CREs even for the most luminous RHs.

9. NUMBER COUNT IN THE ASKAP ERA

We have focused on the RH population detectable with NVSS sensitivity. The RHLF in Section 5.5 indicates a large number of RHs with low luminosities, which would be detectable with future survey with high sensitivity radio telescopes, such as Square Kilometre Array and its pathfinders.

The Australian SKA Pathfinder (ASKAP) is a next generation radio telescope array being built at Murchison Radio-astronomy Observatory in Western Australia (Johnston et al. 2008). It consists of 36 dish antennas, each in 12-m diameter, distributed over with baselines up to 6 km. Its array configuration balances the need for high sensitivity to extended structures with the need for high resolution for continuum projects such as EMU, the "Evolutionary Map of the Universe" (Norris et al. 2011). The short-spacing *uv*-coverage of the ASKAP array has higher sensitivity to extended structures such as cluster RHs. The EMU survey is expected to achieve the sky coverage (75%) similar to the NVSS survey (Condon et al. 1998) but with 45 times better sensitivity.

We use the model explained in Section 5 to calculate the RH population observable with the ASKAP sensitivity. Compared to Section 5, the only modification is the observational limit; we here use the flux-based criterion (Eq. (32)) with $\theta_b = 25$ arcsec, $F_{\text{rms}} = 10 \mu\text{Jy}$ and $\zeta_2 = 10$, following the previous study (Cassano et al. 2012). For the criteria for the RH onset, we here only discuss the *mass-ratio* condition with the parameters listed in Table 2. The luminosity evolution and its mass dependence are unchanged.

In the left panel of Figure 14, we show the mass trend of f_{RH} within $0.05 < z < 0.5$. The fraction f_{RH} at lower mass bins, where the radio power is relatively small, is larger than the values in Figure 7. The mass trend seems similar between the secondary (red) and the primary (blue) scenarios. In the right panel of Figure 14, we show the cumulative number count of RHs as a function of the flux value. Compared to Figure 9, the minimum flux is reduced from $f_{1.4}^{\text{min}} \approx 15$ mJy to 0.3 mJy due to the high sensitivity of ASKAP. We can expect that the ASKAP survey will detect 10^3 RHs, while only ≈ 30 RHs are available with NVSS. Since the RHLF (Figure 8) is a steep function of the luminosity (Figure 5), the number count is dominated by the low-power systems ($P_{1.4} \lesssim 3 \times 10^{23} h_{70}^{-2} \text{ W/Hz}$).

In Figure 15, we show the cumulative number count of RHs for models (i) and (ii). Most of RHs are expected to be found in $z < 0.5$. The cluster mass corresponding to the minimum luminosity observable with the ASKAP sensitivity is $M_{500} \approx 2 \times 10^{14} M_{\odot}$. For $z > 0.5$, the cut-off mass of the HMF becomes smaller than the above threshold mass. Thus, the RH detection at $z > 0.5$ becomes inefficient.

Although the onset conditions are considerably different between models (i) and (ii), f_{RH} and the number count show similar trends. The results look very similar as in Figure 8. This indicates that the survey at a single frequency is not enough to determine the CRE origin in RHs. A multi-band analysis ranging from ≈ 100 MHz to ≈ 10 GHz is important for further discussions. Especially at higher frequencies, where the CRE cooling is more efficient and the RH lifetime is expected even shorter in the primary scenario, the difference between those scenarios could be more apparent. In addition to the radio properties, the statistics of the merger mass ratio, which can be constrained from the X-ray and near-IR band observations, must be important, since it differs much between those scenarios (Section 5).

10. CONCLUSIONS

An increasing number of RHs have been found in recent radio observations of galaxy clusters. The correlation between RHs and dynamically disturbed clusters supports the scenario where the RH emission is powered by the reacceleration of CRs by the merger-induced turbulence, but the origin of the seed CREs for the reacceleration is still poorly constrained. In this study, we compare two possibilities for the origin; the secondary scenario, where the seed population is provided as secondary particles injected via the pp collision, and the primary scenario, where most of the seed CREs are originated from the background thermal electrons and the secondary injection from the pp collision is negligible.

We have solved the FP equations to follow the evolution of the CR distribution in RHs. Our calculation method is basically the same as the one in Nishiwaki et al. (2021), but we have newly included the radial dependence of the reacceleration efficiency in this paper. The radio and gamma-ray observations of the Coma cluster is used to constrain the model parameters. Assuming that the primary CRs are injected with the same radial profile as the thermal gas density, we have found that the radially increasing efficiency of the reacceleration reproduces both the radial profile and the spectrum of the Coma RH under the gamma-ray limit given by *Fermi*-LAT.

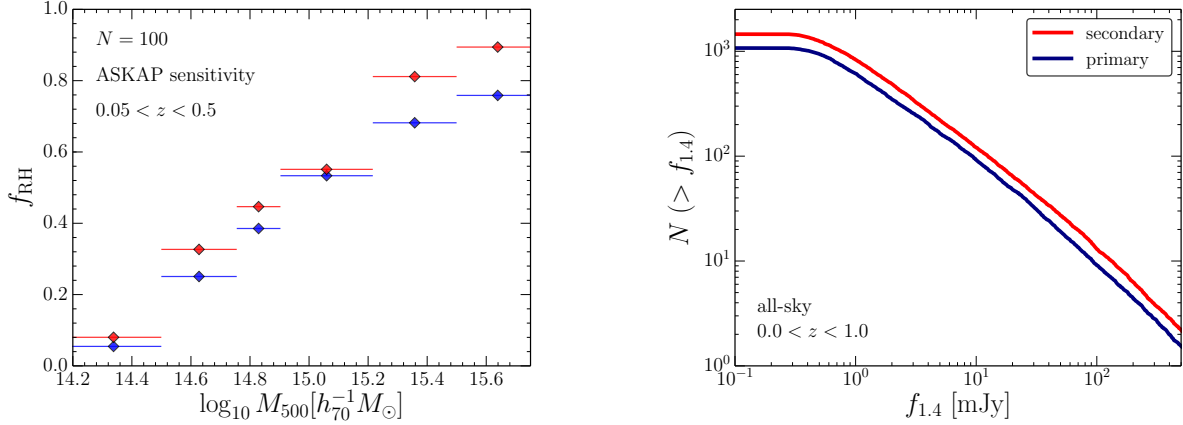


Figure 14. Left: RH fraction with the ASKAP sensitivity ($\theta_b = 25$ arcsec and $F_{\text{rms}} = 10 \mu\text{Jy}$) within $0.05 < z < 0.5$. We adopt $\zeta_2 = 10$ and the parameters listed in Table 2 for models (i) and (ii). Right: number count of RHs accumulated with respect to the flux at 1.4 GHz within $0 < z < 1.0$. In both the panels, the red and blue lines show the results for the secondary and the primary scenarios, respectively.

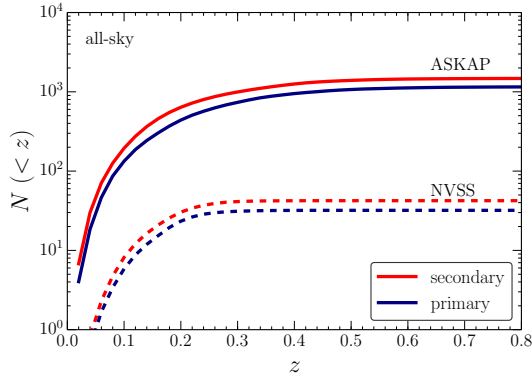


Figure 15. The all-sky number count of RHs observable with ASKAP (solid lines) and NVSS (dashed lines), accumulated with respect to redshift.

Our model calibrated by the Coma RH is then used to study the lifetime of RHs in Section 3. We have followed the evolution in the cooling phase, where the reacceleration ceases. The main results in this part are summarized as follows:

- There are two factors that powers the radio emission: the reacceleration of the seed CREs and the enhanced secondary injection from reaccelerated CRPs.
- In the secondary scenario, a substantial part of the emission is produced by the injection from reaccelerated CRPs. This emission lasts much longer than the cooling timescale of CREs.
- In the primary scenario, the RH emission decays within the cooling timescale ($t_{\text{cool}} \approx 300$ Myr).

- The reacceleration boosts the radio power almost two order of magnitude larger. Thus, we can clearly distinguish radio-loud and radio-quiet clusters.

Based on the merger tree provided in Section 4, we have studied the occurrence conditions of RHs to satisfy the observed RH statistics (Section 5). The most important update from previous studies is the inclusion of the emission lifetime studied in Section 3. We introduce the two conditions for the onset of RHs: *mass-ratio condition* and *break-frequency condition*. The former condition is expressed with the threshold mass ratio, ξ_{RH} , while the latter has two parameters, i.e., the break frequency, ν_b , and the fraction of the turbulent energy to the merger kinetic energy, η_t .

Our results in Sections 5-9 can be summarized as follows:

- The observed fraction and number counts of RHs could be explained in both the two scenarios, but the required threshold value for the merger mass ratio ξ_{RH} differs very much: $\xi_{\text{RH}} \approx 0.25$ and $\xi_{\text{RH}} \approx 0.01$ are required for the secondary and the primary scenarios, respectively.
- The present Coma RH should be in the middle of the luminosity growth due to the reacceleration. The Coma-like RH would achieve its peak luminosity of $P_{1.4} \approx 10^{25}$ W/Hz at an elapsed time ≈ 600 Myr and 700 Myr after the onset of the reacceleration in the secondary and the primary scenarios, respectively.
- A correlation between the halo mass and the peak radio luminosity is required. This correlation

can be reproduced by the mass dependence of the acceleration timescale ($\tau_{\text{acc}} \propto M^{-1/3}$) and a constant duration timescale of the reacceleration. Those parameter behaviors can be justified by a simple model as discussed in Appendix B.

- In order to reproduce the tight correlation between the RHs and the dynamical disturbance seen in the X-ray morphology, the threshold mass ratio to induce the merger signature in X-ray observation should be close to ξ_{RH} . For the primary scenario, this condition requires that even minor mergers with a mass ratio $\xi \approx 0.01$ should produce observable global disturbances.
- Even for the nearest RH in Coma and the brightest RH in Abell 2744, the secondary model can reproduce the observed properties without conflict with the gamma-ray upper limits.
- The RH fraction steeply decreases with decreasing halo mass. However, our model predicts a large number of RHs below the present observable flux limit. The future surveys such as ASKAP are expected to detect ~ 1000 RHs below redshift 0.5 for both the secondary and the primary models.

In summary, we have found that both the secondary and primary models for the origins of the seed CREs are allowed from the current RH statistics. Both the models have both merits and demerits. The secondary scenario requires only major mergers for the RH onset, which is consistent with the fact that RH clusters tend to show

observable morphological disturbance. However, for the Coma RH, the secondary model requires a steeper injection spectral index compared to the primary scenario (see Appendix A). That requirement is even severer for USSRHs, and the CRP energy density possibly exceeds that of the thermal ICM for such RHs in the absence of the reacceleration (e.g., Brunetti et al. 2008). On the other hand, the primary scenario provides a better fit to the Coma spectrum with a flatter injection index and potentially explains USSRHs without requiring an extremely high CR energy density. However, the short lifetime in this scenario requires frequent onsets with $\xi \approx 0.01$ mergers, which is one order of magnitude smaller than the typical value estimated in RH clusters (e.g., Cassano et al. 2016). The required efficiency for the turbulence excitation is relatively high in the primary model to explain the acceleration time of ≈ 300 Myr within the formulation of Appendix B. Either an extended study dedicated for the RH population in lower (≈ 100 MHz) and higher frequencies (≈ 10 GHz), or a statistical analysis of the merger mass ratio of RHs would further constrain the origin of relativistic electrons in the ICM.

ACKNOWLEDGMENTS

K.N. acknowledges the support by the Forefront Physics and Mathematics Program to Drive Transformation (FoPM). This work is supported by the joint research program of the Institute for Cosmic Ray Research (ICRR), the University of Tokyo.

APPENDIX

A. SECONDARY SCENARIO WITH A STEEPER INDEX

As discussed in Section 2.5, our secondary model shows a slight tension with the observed radio flux of Coma above 1 GHz. In this section, we discuss the possibility that this tension could be relaxed when we adopt a steeper injection index α_{inj} .

We have tested the case of $\alpha_{\text{inj}} = 2.45, 2.6, 2.8$ and 3.0 . Since the spectral shape of the synchrotron emission is mostly determined by $t_{\text{R}}/t_{\text{acc}}$ (Nishiwaki et al. 2021), the parameter $t_{\text{acc}}(r_{\text{c}})$ was fixed to 310 Myr. From the gamma-ray upper limit, the lower limit of t_{R} is constrained as $t_{\text{R}} > 0.8t_{\text{acc}}(r_{\text{c}})$. For the turbulent profile, we firstly test the case of $\alpha_{\text{turb}} = 0.28$, i.e. the same value as that in Section 2.5. However, we find that this profile overproduces the 350 MHz intensity at $r > 500$ kpc for $t_{\text{R}} > 0.8t_{\text{acc}}(r_{\text{c}})$. A model with a flat-

ter profile of $\alpha_{\text{turb}} = 0.35$ is compatible with both the radio profile and the gamma-ray limit. Finally, from the radio spectrum, we constrain $t_{\text{R}} = 310$ Myr, i.e., $t_{\text{R}}/t_{\text{acc}}(r_{\text{c}}) = 1.0$. Figure 16 shows the synchrotron spectrum of the best fit model with $\alpha_{\text{inj}} = 3.0$. The observed spectrum is well fitted with the injection luminosity of $L_{\text{p}}^{\text{inj}} = 1.9 \times 10^{44}$ (solid line). The CR energy density in $r < 0.5R_{500}$ becomes $\epsilon_{\text{CR}}/\epsilon_{\text{th}} \approx 0.013$, where ϵ_{th} is the thermal energy density averaged within $r < 0.5R_{500}$. The fraction increases to $\epsilon_{\text{CR}}/\epsilon_{\text{th}} \approx 0.05$ at the peak state ($t_{\text{R}} \approx 500$ Myr).

Throughout this paper, we have assumed $r_{\text{ap}} = 500$ kpc for the aperture radius to calculate the radio spectrum. With this assumption, the overall normalization of the 350 MHz profile becomes consistent with the flux around 350 MHz. In general, the fluxes at other frequencies are taken from different observations and thus

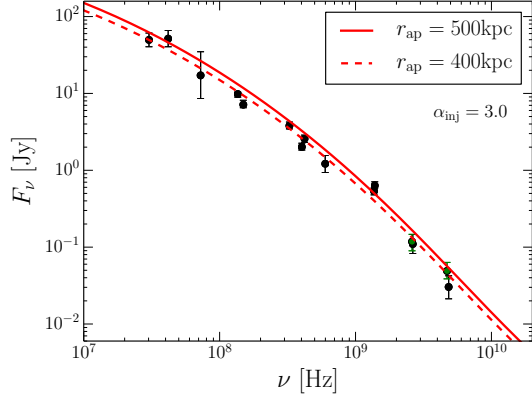


Figure 16. Synchrotron spectra of the Coma RH for the secondary scenario with $\alpha_{\text{inj}} = 3.0$ (solid: $r_{\text{ap}} = 500$ kpc, dashed: $r_{\text{ap}} = 400$ kpc).

originally measured with different aperture radii. We have not taken into account the systematic uncertainty in the re-scaling of those fluxes to $r_{\text{ap}} = 500$ kpc.

By assuming different r_{ap} , we test the case when the normalization is not anchored to the flux at 350 MHz. Assuming $r_{\text{ap}} = 400$ kpc, the calculated flux slightly shifts down and the fit to the data points at high frequency is slightly improved (dashed line).

B. REACCELERATION EFFICIENCY IN THE BINARY MERGER APPROXIMATION

In this section, we discuss the efficiency of the turbulent reacceleration triggered by a cluster merger. As explained in Section 5, we adopt the binary merger approximation. The mass of the descendant halo and the merger mass ratio are denoted as M and $\xi = M_2/M_1$, respectively. The impact parameter is assumed to be zero for simplicity. We especially focus on the CR acceleration by TTD with compressible turbulence. As assumed in Section 2.3, the interaction between turbulence and particles is assumed to be fully collisionless. In this case, the damping of compressible turbulence is dominated by TTD with thermal particles, and the expression of Eq. (10) is applicable. The discussion below is based on the one-zone approximation, unlike in Section 2.3, where we have considered the radial dependence.

To quantify the turbulent energy induced by mergers, we introduce a parameter η_t , which denotes the fraction of the turbulence energy dissipated from the merger kinetic energy. With the volume of the turbulent region V_t , the turbulent energy density is written as $\epsilon_t = \eta_t GM_1 M_2 / R_{\text{mer}} / V_t$, where R_{mer} is the distance between the centers at the impact. Following Cassano & Brunetti (2005), we choose $R_{\text{mer}} = R_1$, i.e., the physical radius of the major progenitor. Eq. (13) provides the radius of the cluster. Cassano & Brunetti (2005)

evaluates V_t from the comparison between typical radius of the RHs and the stripping radius, where the ram pressure experienced by the minor progenitor becomes comparable to its static ICM pressure. We adopt a more simplified approach, $V_t \approx \frac{4\pi}{3}(R_1 R_2)^{3/2}$, assuming that V_t increases with both M_1 and M_2 . The ξ dependence of ϵ_t is affected by the choice of R_{mer} and V_t , while M dependence is not apparently affected, as long as both R_{mer} and V_t are expressed as functions of R_1 and R_2 (or M_1 and M_2).

We can evaluate the turbulent velocity at the scale of the injection from $\rho V_L^2 \approx \epsilon_t$ as,

$$V_L \approx 1.25 \times 10^3 \text{ km/s} \frac{\xi^{\frac{1}{4}}}{(1+\xi)^{\frac{1}{3}}} \left(\frac{M}{10^{15} M_\odot} \right)^{\frac{1}{3}} \times \left(\frac{\eta_t}{0.1} \right)^{1/2} \left(\frac{\Delta}{500} \right)^{\frac{2}{3}} \left(\frac{n}{10^{-3} \text{ cm}^{-3}} \right)^{-\frac{1}{2}}, \quad (\text{B1})$$

where ρ and n are the mass and number densities of the ICM, respectively. The subscript L denotes the injection scale of the turbulence (e.g., Eq. (7)). After a merger with $\xi = 0.2$, the turbulent energy density in the cluster with $M_{500} = 1.0 \times 10^{15} M_\odot$ becomes $\approx 40\%$ of the thermal energy density. This fraction is almost independent of the mass, since the mass dependence of the turbulent energy is similar to that of the temperature.

We adopt the IK scaling, and approximate the outer scale of the turbulence as the size of the minor progenitor, i.e. $L \approx R_2$. Under the assumption of collisionless ICM, the damping rate of the turbulence can be written as Eq. (10). Since the ICM is a high-beta plasma, the sound speed c_s and k_{cut} characterize the timescale of TTD. We simply adopt the observed $M - T$ relation (Eq. (33)) to calculate c_s for different masses. Because the observed relation is similar to the expectation from the virial theorem, $T \propto M^{2/3}$, the turbulent Mach number is nearly independent of the mass.

Above assumptions lead to the scaling of $D_{pp} \propto \xi^{-2/3}(1+\xi)M^{1/3}$. The acceleration timescale, $t_{\text{acc}} = p^2/4D_{pp}$, is plotted in Figure 17 (left panels). The mass dependence is slightly weaker than $M^{1/3}$, since the integral $I_\theta(c_s/c)$ (Eq. (9)) has a weak dependence on c_s . The typical acceleration timescale assumed in Section 7, $t_{\text{acc}} \approx 250$ Myr, could be reproduced with $\eta_t = 0.15$ and $\xi = 0.2$ (solid line in the upper left panel). To achieve a similar acceleration efficiency with $\xi = 0.01$ mergers, the efficiency of turbulent excitation should be as large as $\eta_t \approx 0.4$ (green dashed line).

In Section 7, we have shown that the steep mass dependence in the observed $P_{1.4} - M_{500}$ relation could be explained by the reacceleration with a constant duration. One possible explanation for this model is that

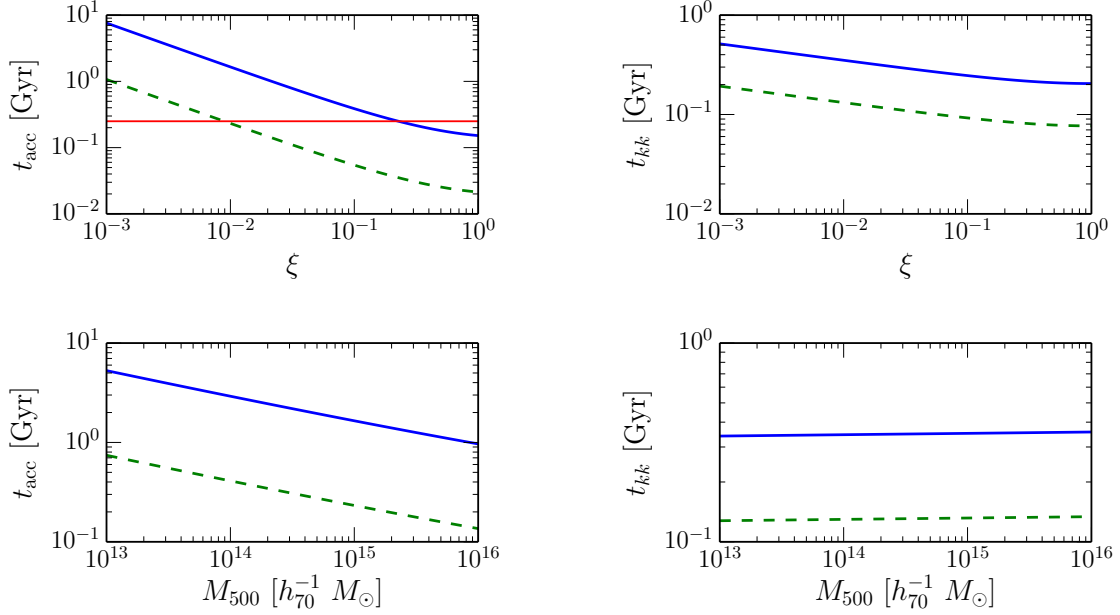


Figure 17. Timescales t_{acc} (left panels) and t_{kk} (right panels) as functions of M_{500} and ξ . The blue solid lines are results for $M_{500} = 1.0 \times 10^{15} M_{\odot}$ (upper panels) and $\xi = 0.1$ (lower panels) with $\eta_t = 0.15$ and $n = 10^{-3} \text{ cm}^{-3}$. The green dashed lines show the results for $\eta_t = 0.40$ with the same values for the other parameters. The red horizontal line in the upper left panel shows the typical acceleration time scale for $M_{500} = 1.0 \times 10^{15} M_{\odot}$ assumed in Section 7.

the duration is regulated by the timescale of the turbulent cascade, t_{kk} , rather than that of the dynamical motion that injects turbulence. The cascade timescale at the injection scale can be expressed as (Brunetti & Lazarian 2007),

$$t_{kk} = \frac{k^3}{\frac{\partial}{\partial k}(k^2 D_{kk})},$$

$$\approx 0.2 \text{ Gyr} \left(\frac{L}{0.5 \text{ Mpc}} \right) \left(\frac{V_L}{10^3 \text{ km/s}} \right)^{-1} \left(\frac{M_s}{0.5} \right)^{-1} \quad (\text{B2})$$

where Eq. (7) is used for D_{kk} . Adopting the same models for L and V_L as that adopted for t_{acc} , one can find the scaling of $t_{kk} \propto \xi^{-1/6}(1 + \xi)^{-1}M^0$. The duration adopted in Section 7, $t_R \approx 500 \text{ Myr}$, corresponds to $2\text{-}3 \times t_{kk}$ for $\xi = 0.1$.

C. MODEL FOR THE A2744 RH

In Section 7, we have extended our models for the Coma RH to other RHs. That model is also used in

Section 8 to discuss the possible constraints from the gamma-ray observation of A2744. In this section, we compare our model with the observed radio spectrum and the brightness profile of A2744.

Figure 18 shows the synchrotron spectrum and the brightness profile at 675 MHz. The data points are adopted from Rajpurohit et al. (2021). We have assumed that the luminosity of the RH has just reached its peak at the observation epoch. Other model parameters and the assumptions are summarized in Section 8.2. The decline of the surface brightness around $r \approx 400 \text{ kpc}$ is also reproduced, although the integrated flux is factor ≈ 2 smaller. Our secondary model well reproduces the radio flux, even though this model is basically extrapolated from the model for the Coma RH.

REFERENCES

- Abdollahi, S., Acero, F., Ackermann, M., et al. 2020, ApJS, 247, 33, doi: [10.3847/1538-4365/ab6bcb](https://doi.org/10.3847/1538-4365/ab6bcb)
- Ackermann, M., Ajello, M., Allafort, A., et al. 2010, ApJL, 717, L71, doi: [10.1088/2041-8205/717/1/L71](https://doi.org/10.1088/2041-8205/717/1/L71)
- Ackermann, M., Ajello, M., Albert, A., et al. 2014, The Astrophysical Journal, 787, 18, doi: [10.1088/0004-637x/787/1/18](https://doi.org/10.1088/0004-637x/787/1/18)

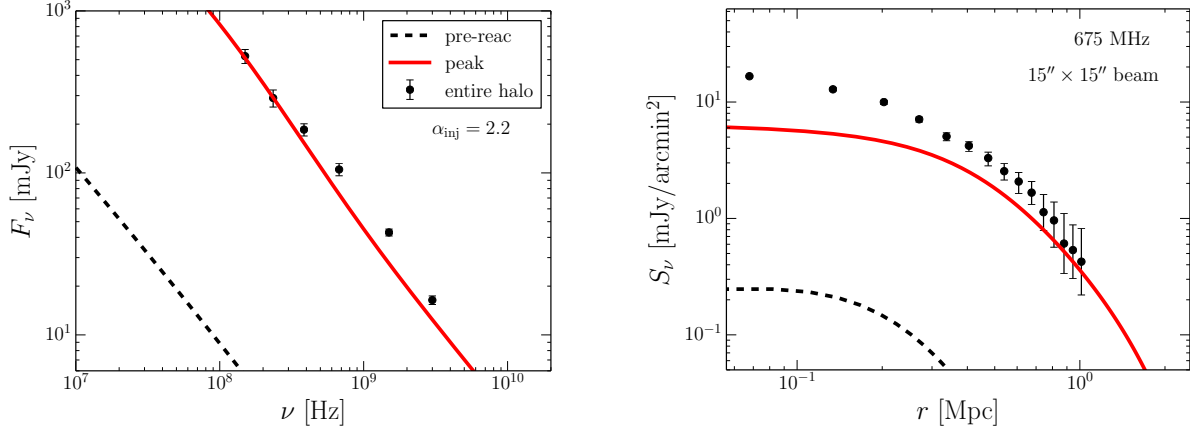


Figure 18. Spectrum (left) and brightness profile (right) of the synchrotron emission from A2744 RH. The model results (solid lines) are from the secondary model adopted in Section 8. We adopt $t_R = 620$ Myr, $\tau_{acc} = 230$ Myr, and the central magnetic field of $B_0 = 4.7 \mu\text{G}$. The Dashed lines show the results in the pre-reacceleration phase ($t_R = 0$ Myr).

- . 2016, *The Astrophysical Journal*, 819, 149,
doi: [10.3847/0004-637x/819/2/149](https://doi.org/10.3847/0004-637x/819/2/149)
- Adam, R., Goksu, H., Brown, S., Rudnick, L., & Ferrari, C. 2021, *A&A*, 648, A60, doi: [10.1051/0004-6361/202039660](https://doi.org/10.1051/0004-6361/202039660)
- Allen, S. W., Rapetti, D. A., Schmidt, R. W., et al. 2008, *MNRAS*, 383, 879, doi: [10.1111/j.1365-2966.2007.12610.x](https://doi.org/10.1111/j.1365-2966.2007.12610.x)
- Angelinelli, M., Vazza, F., Giocoli, C., et al. 2020, *MNRAS*, 495, 864, doi: [10.1093/mnras/staa975](https://doi.org/10.1093/mnras/staa975)
- Blasi, P., & Colafrancesco, S. 1999, *Astroparticle Physics*, 12, 169, doi: [10.1016/S0927-6505\(99\)00079-1](https://doi.org/10.1016/S0927-6505(99)00079-1)
- Bonafede, A., Feretti, L., Murgia, M., et al. 2010, *Astronomy and Astrophysics*, 513, 1,
doi: [10.1051/0004-6361/200913696](https://doi.org/10.1051/0004-6361/200913696)
- Bond, J. R., Cole, S., Efsthathiou, G., & Kaiser, N. 1991, *ApJ*, 379, 440, doi: [10.1086/170520](https://doi.org/10.1086/170520)
- Briel, U. G., Henry, J. P., & Boehringer, H. 1992, *A&A*, 259, L31
- Brunetti, G., & Blasi, P. 2005, *Monthly Notices of the Royal Astronomical Society*, 363, 1173,
doi: [10.1111/j.1365-2966.2005.09511.x](https://doi.org/10.1111/j.1365-2966.2005.09511.x)
- Brunetti, G., & Jones, T. W. 2014, *International Journal of Modern Physics D*, 23, 1,
doi: [10.1142/S0218271814300079](https://doi.org/10.1142/S0218271814300079)
- Brunetti, G., & Lazarian, A. 2007, *Monthly Notices of the Royal Astronomical Society*, 378, 245,
doi: [10.1111/j.1365-2966.2007.11771.x](https://doi.org/10.1111/j.1365-2966.2007.11771.x)
- . 2011, *Monthly Notices of the Royal Astronomical Society*, 412, 817, doi: [10.1111/j.1365-2966.2010.17937.x](https://doi.org/10.1111/j.1365-2966.2010.17937.x)
- Brunetti, G., Setti, G., Feretti, L., & Giovannini, G. 2001, *MNRAS*, 320, 365, doi: [10.1046/j.1365-8711.2001.03978.x](https://doi.org/10.1046/j.1365-8711.2001.03978.x)
- Brunetti, G., Venturi, T., Dallacasa, D., et al. 2007, *ApJL*, 670, L5, doi: [10.1086/524037](https://doi.org/10.1086/524037)
- Brunetti, G., Zimmer, S., & Zandanel, F. 2017, *Monthly Notices of the Royal Astronomical Society*, 472, 1506,
doi: [10.1093/MNRAS/STX2092](https://doi.org/10.1093/MNRAS/STX2092)
- Brunetti, G., Giacintucci, S., Cassano, R., et al. 2008, *Nature*, 455, 944, doi: [10.1038/nature07379](https://doi.org/10.1038/nature07379)
- Buote, D. A. 2001, *ApJL*, 553, L15, doi: [10.1086/320500](https://doi.org/10.1086/320500)
- Cassano, R., & Brunetti, G. 2005, *MNRAS*, 357, 1313,
doi: [10.1111/j.1365-2966.2005.08747.x](https://doi.org/10.1111/j.1365-2966.2005.08747.x)
- Cassano, R., Brunetti, G., Giocoli, C., & Etti, S. 2016, *A&A*, 593, A81, doi: [10.1051/0004-6361/201628414](https://doi.org/10.1051/0004-6361/201628414)
- Cassano, R., Brunetti, G., Norris, R. P., et al. 2012, *A&A*, 548, A100, doi: [10.1051/0004-6361/201220018](https://doi.org/10.1051/0004-6361/201220018)
- Cassano, R., Brunetti, G., Röttgering, H. J. A., & Brüggén, M. 2010, *A&A*, 509, A68,
doi: [10.1051/0004-6361/200913063](https://doi.org/10.1051/0004-6361/200913063)
- Cassano, R., Brunetti, G., & Setti, G. 2006, *MNRAS*, 369, 1577, doi: [10.1111/j.1365-2966.2006.10423.x](https://doi.org/10.1111/j.1365-2966.2006.10423.x)
- Cassano, R., Etti, S., Brunetti, G., et al. 2013, *ApJ*, 777, 141, doi: [10.1088/0004-637X/777/2/141](https://doi.org/10.1088/0004-637X/777/2/141)
- Cho, J., & Lazarian, A. 2003, *MNRAS*, 345, 325,
doi: [10.1046/j.1365-8711.2003.06941.x](https://doi.org/10.1046/j.1365-8711.2003.06941.x)
- Churazov, E., Vikhlinin, A., Zhuravleva, I., et al. 2012, *MNRAS*, 421, 1123,
doi: [10.1111/j.1365-2966.2011.20372.x](https://doi.org/10.1111/j.1365-2966.2011.20372.x)
- Condon, J. J., Cotton, W. D., Greisen, E. W., et al. 1998, *AJ*, 115, 1693, doi: [10.1086/300337](https://doi.org/10.1086/300337)
- Cuciti, V., Cassano, R., Brunetti, G., et al. 2015, *A&A*, 580, A97, doi: [10.1051/0004-6361/201526420](https://doi.org/10.1051/0004-6361/201526420)
- . 2021a, *A&A*, 647, A50,
doi: [10.1051/0004-6361/202039206](https://doi.org/10.1051/0004-6361/202039206)
- . 2021b, *A&A*, 647, A51,
doi: [10.1051/0004-6361/202039208](https://doi.org/10.1051/0004-6361/202039208)
- Dennison, B. 1980, *ApJL*, 239, L93, doi: [10.1086/183300](https://doi.org/10.1086/183300)

- Dewdney, P. E., Hall, P. J., Schilizzi, R. T., & Lazio, T. J. L. W. 2009, *IEEE Proceedings*, 97, 1482, doi: [10.1109/JPROC.2009.2021005](https://doi.org/10.1109/JPROC.2009.2021005)
- Di Gennaro, G., van Weeren, R. J., Brunetti, G., et al. 2021, *Nature Astronomy*, 5, 268, doi: [10.1038/s41550-020-01244-5](https://doi.org/10.1038/s41550-020-01244-5)
- Ebeling, H., Voges, W., Bohringer, H., et al. 1996, *MNRAS*, 281, 799, doi: [10.1093/mnras/281.3.799](https://doi.org/10.1093/mnras/281.3.799)
- Enßlin, T. A., & Röttgering, H. 2002, *A&A*, 396, 83, doi: [10.1051/0004-6361:20021382](https://doi.org/10.1051/0004-6361:20021382)
- Fakhouri, O., Ma, C.-P., & Boylan-Kolchin, M. 2010, *MNRAS*, 406, 2267, doi: [10.1111/j.1365-2966.2010.16859.x](https://doi.org/10.1111/j.1365-2966.2010.16859.x)
- Fujita, Y., Takizawa, M., & Sarazin, C. L. 2003, *ApJ*, 584, 190, doi: [10.1086/345599](https://doi.org/10.1086/345599)
- Giacintucci, S., Markevitch, M., Cassano, R., et al. 2017, *ApJ*, 841, 71, doi: [10.3847/1538-4357/aa7069](https://doi.org/10.3847/1538-4357/aa7069)
- Giovannini, G., Bonafede, A., Feretti, L., et al. 2009, *A&A*, 507, 1257, doi: [10.1051/0004-6361/200912667](https://doi.org/10.1051/0004-6361/200912667)
- Giovannini, G., Tordi, M., & Feretti, L. 1999, *NewA*, 4, 141, doi: [10.1016/S1384-1076\(99\)00018-4](https://doi.org/10.1016/S1384-1076(99)00018-4)
- Gitti, M., Brunetti, G., & Setti, G. 2002, *A&A*, 386, 456, doi: [10.1051/0004-6361:20020284](https://doi.org/10.1051/0004-6361:20020284)
- Govoni, F., Feretti, L., Giovannini, G., et al. 2001, *A&A*, 376, 803, doi: [10.1051/0004-6361:20011016](https://doi.org/10.1051/0004-6361:20011016)
- Govoni, F., Markevitch, M., Vikhlinin, A., et al. 2004, *The Astrophysical Journal*, 605, 695, doi: [10.1086/382674](https://doi.org/10.1086/382674)
- Heinz, S., Brüggen, M., Young, A., & Levesque, E. 2006, *MNRAS*, 373, L65, doi: [10.1111/j.1745-3933.2006.00243.x](https://doi.org/10.1111/j.1745-3933.2006.00243.x)
- Hillas, A. M. 1984, *ARA&A*, 22, 425, doi: [10.1146/annurev.aa.22.090184.002233](https://doi.org/10.1146/annurev.aa.22.090184.002233)
- Ibaraki, Y., Ota, N., Akamatsu, H., Zhang, Y. Y., & Finoguenov, A. 2014, *A&A*, 562, A11, doi: [10.1051/0004-6361/201322806](https://doi.org/10.1051/0004-6361/201322806)
- Jeltema, T. E., & Profumo, S. 2011, 728, 53, doi: [10.1088/0004-637x/728/1/53](https://doi.org/10.1088/0004-637x/728/1/53)
- Jenkins, A., Frenk, C. S., White, S. D. M., et al. 2001, *MNRAS*, 321, 372, doi: [10.1046/j.1365-8711.2001.04029.x](https://doi.org/10.1046/j.1365-8711.2001.04029.x)
- Johnston, S., Taylor, R., Bailes, M., et al. 2008, *Experimental Astronomy*, 22, 151, doi: [10.1007/s10686-008-9124-7](https://doi.org/10.1007/s10686-008-9124-7)
- Kale, R., Venturi, T., Giacintucci, S., et al. 2013, *A&A*, 557, A99, doi: [10.1051/0004-6361/201321515](https://doi.org/10.1051/0004-6361/201321515)
- Kamae, T., Karlsson, N., Mizuno, T., Abe, T., & Koi, T. 2006, *The Astrophysical Journal*, 680, 224, doi: [10.1086/587449](https://doi.org/10.1086/587449)
- Kang, H., Ryu, D., & Jones, T. W. 2012, *ApJ*, 756, 97, doi: [10.1088/0004-637X/756/1/97](https://doi.org/10.1088/0004-637X/756/1/97)
- Kushnir, D., & Waxman, E. 2009, *JCAP*, 2009, 002, doi: [10.1088/1475-7516/2009/08/002](https://doi.org/10.1088/1475-7516/2009/08/002)
- Lacey, C., & Cole, S. 1993, *MNRAS*, 262, 627, doi: [10.1093/mnras/262.3.627](https://doi.org/10.1093/mnras/262.3.627)
- Lewis, A., Challinor, A., & Lasenby, A. 2000, *ApJ*, 538, 473, doi: [10.1086/309179](https://doi.org/10.1086/309179)
- Macario, G., Venturi, T., Brunetti, G., et al. 2010, *A&A*, 517, A43, doi: [10.1051/0004-6361/201014109](https://doi.org/10.1051/0004-6361/201014109)
- Miniati, F. 2015, *ApJ*, 800, 60, doi: [10.1088/0004-637X/800/1/60](https://doi.org/10.1088/0004-637X/800/1/60)
- Mohr, J. J., Fabricant, D. G., & Geller, M. J. 1993, *ApJ*, 413, 492, doi: [10.1086/173019](https://doi.org/10.1086/173019)
- Nelson, K., Lau, E. T., & Nagai, D. 2014, *Astrophysical Journal*, 792, 25, doi: [10.1088/0004-637X/792/1/25](https://doi.org/10.1088/0004-637X/792/1/25)
- Nishiwaki, K., Asano, K., & Murase, K. 2021, *The Astrophysical Journal*, 922, 190, doi: [10.3847/1538-4357/ac1cdb](https://doi.org/10.3847/1538-4357/ac1cdb)
- Norris, R. P., Hopkins, A. M., Afonso, J., et al. 2011, *PASA*, 28, 215, doi: [10.1071/AS11021](https://doi.org/10.1071/AS11021)
- Ota, N., & Mitsuda, K. 2004, *A&A*, 428, 757, doi: [10.1051/0004-6361:20041087](https://doi.org/10.1051/0004-6361:20041087)
- Petrosian, V. 2001, *ApJ*, 557, 560, doi: [10.1086/321557](https://doi.org/10.1086/321557)
- Pfrommer, C., Enßlin, T. A., & Springel, V. 2008, *MNRAS*, 385, 1211, doi: [10.1111/j.1365-2966.2008.12956.x](https://doi.org/10.1111/j.1365-2966.2008.12956.x)
- Pinzke, A., Oh, S. P., & Pfrommer, C. 2017, *Monthly Notices of the Royal Astronomical Society*, 465, 4800, doi: [10.1093/mnras/stw3024](https://doi.org/10.1093/mnras/stw3024)
- Pinzke, A., & Pfrommer, C. 2010, *Monthly Notices of the Royal Astronomical Society*, 409, 449, doi: [10.1111/j.1365-2966.2010.17328.x](https://doi.org/10.1111/j.1365-2966.2010.17328.x)
- Pizzo, R. F. 2010, PhD thesis, University of Groningen
- Planck Collaboration, Ade, P. A. R., Aghanim, N., et al. 2013, *A&A*, 554, A140, doi: [10.1051/0004-6361/201220247](https://doi.org/10.1051/0004-6361/201220247)
- Planck Collaboration, Aghanim, N., Akrami, Y., et al. 2020, *A&A*, 641, A6, doi: [10.1051/0004-6361/201833910](https://doi.org/10.1051/0004-6361/201833910)
- Press, W. H., & Schechter, P. 1974, *ApJ*, 187, 425, doi: [10.1086/152650](https://doi.org/10.1086/152650)
- Rajpurohit, K., Vazza, F., van Weeren, R. J., et al. 2021, *A&A*, 654, A41, doi: [10.1051/0004-6361/202141060](https://doi.org/10.1051/0004-6361/202141060)
- Rybicki, G. B., & Lightman, A. P. 1985, *Radiative Processes in Astrophysics* (New York, NY: Wiley), doi: [10.1002/9783527618170](https://doi.org/10.1002/9783527618170)
- Santos, J. S., Rosati, P., Tozzi, P., et al. 2008, *A&A*, 483, 35, doi: [10.1051/0004-6361:20078815](https://doi.org/10.1051/0004-6361:20078815)
- Schlickeiser, R. 2002, *Cosmic Ray Astrophysics* (Springer)
- Schuecker, P., Böhringer, H., Reiprich, T. H., & Feretti, L. 2001, *A&A*, 378, 408, doi: [10.1051/0004-6361:20011215](https://doi.org/10.1051/0004-6361:20011215)
- Sheth, R. K., & Tormen, G. 1999, *MNRAS*, 308, 119, doi: [10.1046/j.1365-8711.1999.02692.x](https://doi.org/10.1046/j.1365-8711.1999.02692.x)
- Tinker, J., Kravtsov, A. V., Klypin, A., et al. 2008, *ApJ*, 688, 709, doi: [10.1086/591439](https://doi.org/10.1086/591439)

- van Haarlem, M. P., Wise, M. W., Gunst, A. W., et al. 2013, *A&A*, 556, A2, doi: [10.1051/0004-6361/201220873](https://doi.org/10.1051/0004-6361/201220873)
- van Weeren, R. J., de Gasperin, F., Akamatsu, H., et al. 2019, *SSRv*, 215, 16, doi: [10.1007/s11214-019-0584-z](https://doi.org/10.1007/s11214-019-0584-z)
- Vazza, F., Jones, T. W., Brüggen, M., et al. 2017, *MNRAS*, 464, 210, doi: [10.1093/mnras/stw2351](https://doi.org/10.1093/mnras/stw2351)
- Venturi, T., Giacintucci, S., Brunetti, G., et al. 2007, *A&A*, 463, 937, doi: [10.1051/0004-6361:20065961](https://doi.org/10.1051/0004-6361:20065961)
- Vikhlinin, A., Kravtsov, A., Forman, W., et al. 2006, *ApJ*, 640, 691, doi: [10.1086/500288](https://doi.org/10.1086/500288)
- Völk, H. J., & Atoyan, A. M. 1999, *Astroparticle Physics*, 11, 73, doi: [10.1016/S0927-6505\(99\)00029-8](https://doi.org/10.1016/S0927-6505(99)00029-8)
- Watson, W. A., Iliev, I. T., D’Aloisio, A., et al. 2013, *MNRAS*, 433, 1230, doi: [10.1093/mnras/stt791](https://doi.org/10.1093/mnras/stt791)
- Xi, S.-Q., Wang, X.-Y., Liang, Y.-F., et al. 2018, *PhRvD*, 98, 063006, doi: [10.1103/PhysRevD.98.063006](https://doi.org/10.1103/PhysRevD.98.063006)
- Yuan, Z. S., Han, J. L., & Wen, Z. L. 2015, *ApJ*, 813, 77, doi: [10.1088/0004-637X/813/1/77](https://doi.org/10.1088/0004-637X/813/1/77)
- Zandanel, F., Pfrommer, C., & Prada, F. 2014, *Monthly Notices of the Royal Astronomical Society*, 438, 124, doi: [10.1093/mnras/stt2250](https://doi.org/10.1093/mnras/stt2250)